JOURNAL OF PETROLOGY | VOLUME 53 | NUMBER 3 | PAGES 477–511 | 2012 | doi:10.1093/petrology/egr069

Deep Lithospheric Thickening and Refertilization beneath Continental Arcs: Case Study of the *P*, *T* and Compositional Evolution of Peridotite Xenoliths from the Sierra Nevada, California

EMILY J. CHIN[1]*, CIN-TY A. LEE[1], PETER LUFFI[1] AND MIKE TICE[2]

[1]DEPARTMENT OF EARTH SCIENCE, RICE UNIVERSITY MS-126, 6100 MAIN STREET, HOUSTON, TX 77005, USA

[2]DEPARTMENT OF GEOLOGY AND GEOPHYSICS, MS 3115, TEXAS A&M UNIVERSITY, COLLEGE STATION, TX 77843, USA

RECEIVED JANUARY 1, 2011; ACCEPTED NOVEMBER 18, 2011

Thickening of arc lithosphere influences the extent of magmatic differentiation and is thereby important for the evolution of juvenile arcs into mature continental crust. Here, we use mantle xenoliths from the late Mesozoic Sierra Nevada continental arc in California (USA) to constrain the pressure, temperature, and compositional evolution of the deep lithosphere beneath a mature arc. These xenoliths consist of spinel peridotites and garnet-bearing spinel peridotites. The former are characterized by coarse-grained protogranular textures having bulk compositions indicative of high-degree melting. The latter are characterized by porphyroclastic textures, garnet coronas around spinels, garnet exsolution lamellae in pyroxenes, and pyroxenes with high-Al cores and low-Al rims. The garnet-bearing spinel peridotites range from depleted to fertile compositions, but the high Cr-numbers [molar Cr/(Cr+Al)] of spinel cores reflect high-degree melting. These observations suggest that the protoliths of the garnet-bearing spinel peridotites were melt-depleted spinel peridotites. Constraints from geothermobarometry and bulk compositions coupled with mantle melting models suggest that the protoliths underwent shallow melt depletion (1–2 GPa, 1300–1400°C), followed by compression, cooling, and final equilibration within the garnet stability field (~3 GPa, <800°C). The deepest equilibrated samples are the most refertilized, suggesting that refertilization occurred during compression. We interpret this P–T*–composition path to reflect progressive thickening of the Sierran arc lithosphere perhaps as a result of magmatic inflation or tectonic thickening. We hypothesize that newly formed arc lithospheric mantle thickens enough to pinch out the asthenospheric wedge, juxtaposing Sierran arc lithosphere against the subducting oceanic plate. This could have terminated arc magmatism and initiated cooling of the deep Sierran lithosphere.*

KEY WORDS: *continental arc lithosphere; peridotite; xenolith; Sierra Nevada*

INTRODUCTION

Island and continental arcs are the dominant building blocks of Phanerozoic continents. It is in such environments that the felsic composition of average continental crust is achieved. Melting of the asthenospheric mantle wedge beneath arc volcanoes by decompression, volatile fluxing, or a combination of both generates primary arc magmas, leaving behind a depleted mantle residuum that may underplate the overriding lithosphere, and may eventually become incorporated into newly formed lithosphere. Mantle-derived arc magmas rise into the overriding lithosphere, where they cool, crystallize and differentiate into felsic liquids and complementary mafic cumulates and restites. The denser mafic lithologies are believed to be convectively removed and returned into the mantle, whereas the felsic residual liquids crystallize to form the continental crust (Kay & Kay, 1988; Kelemen, 1995; Rudnick, 1995; Ducea & Saleeby, 1996; Rudnick & Gao, 2003; Tatsumi, 2005; Lee *et al.*, 2006; Jagoutz *et al.*, 2009). Extensive magmatic differentiation should be favored in continental arcs or mature island arcs because of the thicker crust and lithospheric mantle through which juvenile basalts must move and interact. Although it is generally thought that differentiation occurs primarily in the crust, as evidenced by the presence of abundant restites and cumulates in the

*Corresponding author. E-mail: ejc5@rice.edu

lower crust (Arndt & Goldstein, 1989; Annen *et al.*, 2006; Lee *et al.*, 2006; Jagoutz *et al.*, 2009), even deeper (e.g. sub-Moho) differentiation might occur in arcs with thicker lithospheres. The depth at which such differentiation occurs will influence the composition of the erupted lavas. For example, deep lithosphere fractionation would modify the composition of magmas well before they traverse the crust–mantle boundary, hence failure to account for this would make mass-balance models of arc crust inaccurate. In addition, deep lithosphere fractionation would also modify the composition of the lithospheric mantle by the addition of deep-seated cumulates or the products of melt–rock reaction (Kelemen, 1990). It is generally thought that continental lithospheric mantle is composed of melt-depleted peridotites (Boyd & Mertzman, 1987; Walter, 1998; Carlson *et al.*, 2005), but extensive differentiation in the deep lithosphere could result in refertilization of such lithosphere.

The purpose of this study is to investigate whether arc lithosphere thickens and, if so, constrain the extent and mechanisms of thickening. Here, we investigate the pressure (P) and temperature (T) evolution of the lithospheric mantle beneath the Sierra Nevada Batholith, a remnant of a Cretaceous ocean–continent subduction zone in western North America (Fig. 1). Although many studies have been conducted on the deep continental crust in arcs (DeBari & Sleep, 1991; Ducea & Saleeby, 1996; Kelemen & Hanghoj, 2003; Lee *et al.*, 2006; Jagoutz *et al.*, 2009), most of these studies do not focus on P–T evolution and none have investigated the lithospheric mantle part of the arc in detail. However, the P–T evolution of the deep arc lithosphere may provide new constraints on the nature of arc thickening. For example, during accretion, compression or underthrusting in continental arcs (Fig. 2a) (Coney & Harms, 1984; DeCelles, 2004; Dickinson, 2004; Ducea & Barton, 2007; DeCelles *et al.*, 2009), the deep lithosphere might be expected to increase in P and T. Interactions with the subducting oceanic lithosphere could also lead to thickening (increase in P) via refrigeration or freezing (decrease in T) of the asthenospheric mantle wedge (Saltzer *et al.*, 2001) (Fig. 2b), although it has also been proposed that too much coupling, such as during low-angle subduction, could erode the lithospheric mantle altogether (see Bird, 1988). Thickening could also occur by underplating of magmas or residual peridotitic mantle to the base of the overriding lithosphere (Fig. 2c) (Jordan, 1981; McDonough, 1990). In this case, the newly underplated material would bear, in theory, a record of initial decompression followed by isobaric cooling. Finally, another way to thicken is by magmatic inflation, wherein progressive intrusion of magmas into the crust displaces underlying parts of the lithosphere to greater depths and pressures, provided erosion at the Earth's surface does not compensate for magmatic addition (Fig. 2d) (Annen *et al.*, 2006). In such a scenario, rapid magmatic inflation might be expected to result in near-adiabatic compression of the deeper portions of the lithosphere (Fig 2d) whereas slow inflation might permit lithospheric geotherms to re-equilibrate such that single parcels of lithosphere would gradually heat up as they become progressively depressed into the hot, underlying asthenosphere.

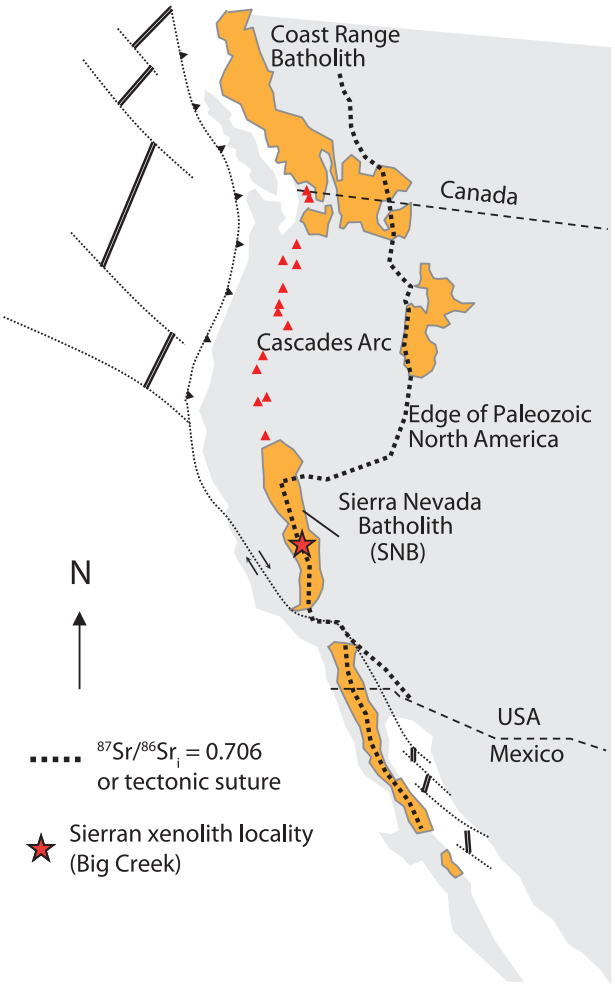

Fig. 1. Simplified map of the western USA showing the location of Mesozoic Cordilleran batholiths and the Big Creek xenolith locality.

To access the deep lithosphere beneath the Sierra Nevada arc, we use peridotite xenoliths entrained in late Miocene alkali basalts. We combine new major and trace element geochemical data for minerals and whole-rocks to constrain the P–T and compositional evolution of the Sierran continental arc lithospheric mantle. We constrain the initial 'leg' of the P–T path using relationships between melting degree (F) recorded by the Sierran peridotites and pressure, which is a proxy for paleo-depth. The final 'leg' is constrained using geothermobarometry, which

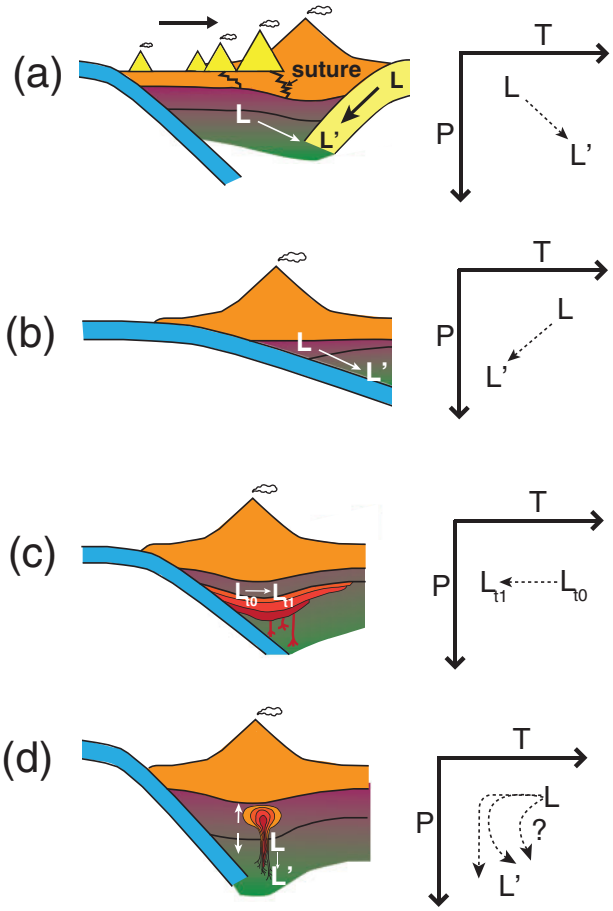

Fig. 2. Schematic illustrations of the potential mechanisms responsible for thickening the continental arc lithosphere. Hypothetical *P*–*T* paths tracking the lithostatic *P* and *T* of a parcel of lithosphere (L) during thickening are shown to the right (L' represents L after thickening has occurred). (See text for discussion.) (a) Arc accretion and continental underthrusting; (b) shallow-angle subduction and viscous coupling of asthenospheric mantle wedge to downgoing slab; (c) lithospheric underplating by magmas or melt-depleted peridotite; (d) magmatic inflation.

gives the final equilibration pressures and temperatures of the peridotites. These constraints on *P*–*T* and compositional evolution add a new perspective to an existing body of work focused on the petrogenesis of Sierran lower crustal and upper mantle xenoliths (Dodge *et al.*, 1988; Mukhopadhyay & Manton, 1994; Ducea & Saleeby, 1996; Lee *et al.*, 2001, 2006; Ducea, 2002) and are used to formulate models for the evolution of continental arcs.

GEOLOGICAL SETTING

Overall geological history

The Sierra Nevada Batholith is a Mesozoic magmatic arc formed by subduction of the Farallon plate beneath North America (Fig. 1). Magmatism occurred between 220 and 80 Ma with its most productive stage occurring between ~120 and 80 Ma, peaking at ~93 Ma (Chen & Moore, 1982; Barton, 1996; Coleman & Glazner, 1997). The Mid- to Late Cretaceous magmatism was accompanied by thin-skinned compressional deformation that extended from the Sierra Nevada east into the present-day Rocky Mountains. This period of deformation, known as the Sevier orogeny (Armstrong, 1968), was characterized by foreland fold-and-thrust belts and possible retro-arc thrusting of North American lithosphere beneath the active Sierran arc (DeCelles, 2004; DeCelles *et al.*, 2009). By ~74 Ma, major arc-building magmatism terminated, and much of western North America entered a period of compressional deformation in the form of basement-cored uplifts known as the Laramide orogeny (Dickinson & Snyder, 1978). The onset of the Laramide orogeny is generally attributed to the shallowing of the downgoing Farallon plate (Coney & Reynolds, 1977; Dickinson & Snyder, 1978; Bird, 1988) or to collision with an oceanic plateau (Saleeby, 2003). During the Laramide orogeny, magmatism appears to have migrated eastward into the continental interior (Coney & Reynolds, 1977; Lipman, 1992) and a cooler thermal regime was imposed on the overriding North American lithosphere, possibly accompanied by extensive hydration and metasomatism (Dumitru *et al.*, 1991; Humphreys *et al.*, 2003; Lee, 2005). At ~40 Ma, much of the Cordilleran orogenic belt began to collapse and magmatism in the form of rhyolitic or ignimbritic flare-ups migrated back towards the west, perhaps owing to the foundering or roll-back of the Farallon plate (Coney & Reynolds, 1977; Humphreys, 1995). Collision of the Pacific–Farallon ridge with the Farallon–North American trench at ~20 Ma resulted in the birth of the San Andreas transform and the opening of a 'slabless window' beneath western North America (Atwater, 1970). Continued collapse of the Cordilleran orogen culminated in extension of the Basin and Range Province, which continues today (Wernicke, 1981). Basin and Range extension appears to have been accompanied by widespread Late Miocene to present basaltic volcanism, including small-volume alkalic to ultrapotassic basalts of Late Miocene to Pleistocene age in the central and eastern Sierra Nevada (Van Kooten, 1980; Dodge *et al.*, 1988). These Sierran volcanic centers contain xenoliths of the deep Sierran crust and lithospheric mantle. The xenoliths investigated here come from the Late Miocene Big Creek diatreme (37°13'N, 119°16'W) erupted at ~8 Ma and now exposed as a small (110 m × 260 m), elliptical trachyandesitic pipe located in the central part of the batholith (Dodge *et al.*, 1988; Ducea & Saleeby, 1998*b*).

The Sierra Nevada Batholith

In the Sierra Nevada Batholith, Kistler & Peterman (1973) and Kistler (1990) noted an east–west transition in lithosphere composition, manifested by a transition from

unradiogenic to radiogenic initial Sr isotopic signatures (the $^{87}Sr/^{86}Sr_i = 0{\cdot}706$ boundary). Mafic granitoids dominate the batholith west of the 0·706 line; these were emplaced into recently accreted oceanic terranes characterized by unradiogenic Sr (low $^{87}Sr/^{86}Sr_i$). Felsic, granitic plutons dominate in the east and appear to have interacted extensively with pre-existing, Precambrian-derived sediments and/or basement (Saleeby *et al.*, 1987), responsible for their radiogenic Sr (high $^{87}Sr/^{86}Sr_i$). In particular, the major and trace element signatures of the plutons in the eastern Sierran and Peninsular Ranges batholiths (the latter represents the southern extension of the Cordilleran magmatic arc) require the presence of garnet-bearing mafic cumulates and restites at depth (Gromet & Silver, 1987). Garnet pyroxenite xenoliths from the lower crust and lithospheric mantle beneath the Sierra Nevada have compositions that match the expected mafic complements to the plutons (Mukhopadhyay & Manton, 1994; Ducea, 2001, 2002; Lee *et al.*, 2006, 2007*b*). Lee *et al.* (2006) subdivided the garnet pyroxenites into two groups, a high-MgO group representing high-pressure (1–3 GPa) cumulates of a primary, hydrous basaltic magma and a low-MgO group, representing cumulates or restites of evolved basalts at lower crustal pressures (~1·5 GPa). This petrogenetic relationship implies that thick crust or lithosphere was needed to generate such deep mafic cumulates and restites because thick lithosphere would force mantle-derived magmas to differentiate at greater depths, facilitating the crystallization of garnet-rich, high-MgO pyroxenites (Sisson *et al.*, 1996; Lee *et al.*, 2006). This garnet pyroxenite root is suggested to have been removed sometime after 10 Ma and before 0·18 Ma (Ducea & Saleeby, 1996, 1998*b*; Farmer *et al.*, 2002; Zandt *et al.*, 2004).

SUMMARY OF PREVIOUS WORK

Xenoliths from the Big Creek diatreme can be broadly categorized into two groups: a mafic group consisting of pyroxenites and granulites from the lower crust and possibly the lithospheric mantle, and an ultramafic group characterized by peridotites associated with the lithospheric mantle (Dodge *et al.*, 1988; Mukhopadhyay & Manton, 1994; Ducea & Saleeby, 1996). The mafic lithologies, as mentioned above, have been interpreted to represent the restites and cumulates complementary to the Sierran granitoids and have been discussed in detail elsewhere (Lee *et al.*, 2006). The peridotites are thought to represent the deepest samples of the sub-continental arc lithosphere, with some recording equilibration pressures up to 3 GPa (Ducea & Saleeby, 1998*a*; Lee *et al.*, 2001). They have undergone various degrees of partial melting, as evidenced by compositions ranging from depleted harzburgites to fertile lherzolites (Mukhopadhyay & Manton, 1994; Lee *et al.*, 2001). In the garnet-bearing spinel peridotites, Lee *et al.* (2001) identified cooling features, such as garnet rimming spinel and garnet exsolution lamellae in pyroxenes. Based on Ca-in-opx geothermometry on garnet-free regions of orthopyroxene, Lee *et al.* showed that initial temperatures of the garnet peridotites were at least 1140°C, whereas final ('closure') temperatures based on orthopyroxene compositions adjacent to garnet lamellae were less than 800°C, thus indicating substantial cooling. However, the possibility of pressure change (ΔP) accompanying cooling was not evaluated. Based on the peridotites' thermal history, isotopic evidence, and comparisons with xenoliths from Quaternary basalts in the Basin and Range, those workers considered the Big Creek peridotites to represent recently upwelled asthenospheric mantle that replaced old, lithospheric mantle during a lithospheric removal or rejuvenation event, possibly related to the Cretaceous arc magmatism itself. We build on these pre-existing studies by presenting detailed petrographic, geothermobarometric and geochemical studies of Sierran peridotite xenoliths, with particular emphasis on garnet-bearing spinel peridotites.

METHODS

Whole-rock major element and trace element contents were determined by X-ray fluorescence spectroscopy (XRF) at Washington State University at Pullman and by inductively coupled plasma mass spectrometry (ICPMS) using a ThermoFinnigan Element 2 system at Rice University. ICPMS sample preparation was as follows. Owing to limited sample size, ≤5 cm chunks of whole-rocks were crushed and powdered in a ceramic SPEX mill placed in a shatterbox for 5–10 min per sample. Care was taken to pick only the freshest, interior portions of the rocks for milling. Sample powder (50–80 mg) was added to a weighed, empty, and dry 2·5 ml Savillex wrench-top beaker. Two sequential acid attacks using a 1:1 mixture of concentrated HF–$HClO_4$ were performed, with complete open-air dry-down at ~190°C between each attack. After the acid attacks, ~1–2 ml of 2% HNO_3 was added to each beaker. Then each beaker was diluted to a total volume of 125 ml by addition of 2% HNO_3, and 0·025 ml of HCl was added to each beaker to keep Fe in solution. Independently prepared standards (BHVO-1, BIR-1, AGV-1, DTS-1, JP-1) were used as external standards using values from Eggins *et al.* (1997). For an internal standard, all solutions were spiked with indium to achieve a 1 ppb concentration of In in solution. Procedural blanks were run in duplicate. Prior to running on the ICPMS system, all samples were ultrasonicated for 30 min and allowed to sit overnight. Na, Mg, Al, P, K, Ca, Sc, Ti, V, Cr, Mn, Fe, Co, Ni, Cu, Zn, Nb, and Zr were analyzed in medium mass resolution mode ('MR-ICPMS', $m/\Delta m = 3000$). Li, Be, Rb, Sr, Y, Cs, Ba, Pb, Th, Ta, Tl, and the rare earth elements (REE) were

analyzed in low mass resolution mode ('LR-ICPMS', $m/\Delta m = 300$).

Major element concentrations of minerals in sample 1026 V were acquired using wavelength-dispersive spectroscopy (WDS) on the JEOL JXA-8530 F 'Hyperprobe' at Yale University. The operating conditions were 15 kV accelerating voltage, probe current of 5·042 nA, and 40 ms dwell time. X-ray maps of orthopyroxene and clinopyroxene in 1026 V were also acquired in WDS mode on the Hyperprobe. X-ray maps were processed offline using ImageJ software (http://rsbweb.nih.gov/ij/). Major element concentrations of minerals in samples 08BC03, 08BC04, 08BC08, and BC-77 were acquired in WDS mode on the Cameca SX 50 at Texas A&M University. On both electron microprobes, typical spot sizes were 1–1·5 μm. Olivine, orthopyroxene, clinopyroxene, garnet, and chromite standards were used.

Energy-dispersive X-ray maps for Cr, Al, and Ca were generated using a Horiba XGT-7000 micro-XRF system at Texas A&M University. Operating conditions were 50 kV accelerating voltage and 1 mA probe current. The mapping image threshold was 10 μm; we used a spot size of 100 μm.

In situ trace element compositions of minerals were obtained using laser ablation ICPMS (ThermoFinnigan Element 2 equipped with New Wave 213 nm laser ablation system) at Rice University. Polished 30 μm thick sections of the peridotites 1026 V and BC-77, and polished 300 μm thick sections of the peridotites 08BC03, 08BC04, 08BC08, and 08BC14 were analyzed. Analyses were performed in low mass resolution mode. The laser beam was set to 55 μm spot size, 10 Hz pulse frequency, and 20 J cm^{-2} energy fluence. ^{25}Mg was used as an internal standard to correct for instrument drift. BHVO2g, BIR1g, BCR2g, and NIST612 basaltic glass standards were used as external standards using standard values from Gao *et al.* (2002). Prior to analysis, the instrument was tuned by manually controlling the sample gas (Ar) to obtain a sensitivity of >300 000 c.p.s. per 15 ppm La in BHVO2g for a 55 μm diameter spot and a pulse frequency of 10 Hz. Time-resolved analyses were converted to concentrations using in-house Excel macros (http://www.ruf.rice.edu/~ctlee/Laser-RAWDATA-TEMPLATE.xls).

RESULTS

General xenolith petrography and textural history

This study focuses on the detailed petrography and geochemistry of five garnet-bearing spinel peridotites out of a suite of 10 garnet-bearing samples: 1026 V, BC-77, 08BC03, 08BC04, and 08BC08 (Figs 3 and 4). Garnet-bearing peridotites provide the most reliable quantitative determination of P–T paths because garnet–pyroxene geothermobarometry can be applied. However, for completeness, we also include less detailed data on spinel peridotites. Although garnet makes up ≥8% by mode in the garnet-bearing spinel peridotites, we refer to them as 'garnet-bearing' because, as we show below, the entire Sierran peridotite suite represents a continuum in terms of textures and geochemistry, the spinel peridotites being the inferred protoliths of the garnet-bearing spinel peridotites.

In order of decreasing abundance, the Sierran peridotites are composed of olivine, orthopyroxene, clinopyroxene, and one or two aluminous phases (spinel and/or garnet). Mineral modes for three spinel peridotites (08BC01, 08BC13, and P7) and five garnet-bearing spinel peridotites (BC77, 1026 V, 08BC03, 08BC04, 08BC08) were calculated using least-squares inversion of the whole-rock and average mineral major element compositions (see Table 1). The sums of the residuals are all ≤0·6 (Table 1), indicating that our sample sizes, although small, are still sufficiently large to average out grain-scale heterogeneity in mineral modes. Spinel peridotites are generally coarse-grained (average grain size 4 mm or greater) and have a protogranular texture (see Mercier & Nicolas, 1975) (Fig. 3). Olivine and orthopyroxene are the dominant minerals in the spinel peridotites, with subordinate clinopyroxene and accessory spinel. Curvilinear grain boundaries are often present between olivine, orthopyroxene, and clinopyroxene (where present) grains (Fig. 3). Spinels in the coarsest samples tend to be large (1–2 mm) and euhedral, whereas spinels in more recrystallized samples show increasing degrees of elongation. Some olivine grains in the spinel peridotites show kink-banding. No clear foliation or shape-preferred orientation of minerals is present in the spinel peridotites.

Representative thin sections, μ-XRF maps, and photomicrographs of garnet-bearing spinel peridotites are presented in Fig. 4. In contrast to spinel peridotites, the garnet-bearing samples are porphyroclastic, and have a weakly foliated fabric defined by shape-preferred orientation of recrystallized olivines (showing unequilibrated grain boundary triple junctions) and diffuse bands of fine-grained clinopyroxene and garnet disseminated within the recrystallized olivine matrix. These diffuse clinopyroxene bands are conspicuous in the μ-XRF maps (shown by green colors), where they often occur together with fine-grained, discrete garnets. Porphyroclasts are composed of orthopyroxene and clinopyroxene; the former are typically highly deformed, and the latter are less deformed. Two samples, 1026 V and BC77, contain exceptionally large (~1 cm), deformed and bent orthopyroxene porphyroclasts. Such porphyroclasts also show extensive kink-banding and bending of cleavage planes. We interpret these orthopyroxene porphyroclasts as relict grains from a coarse-grained harzburgitic protolith.

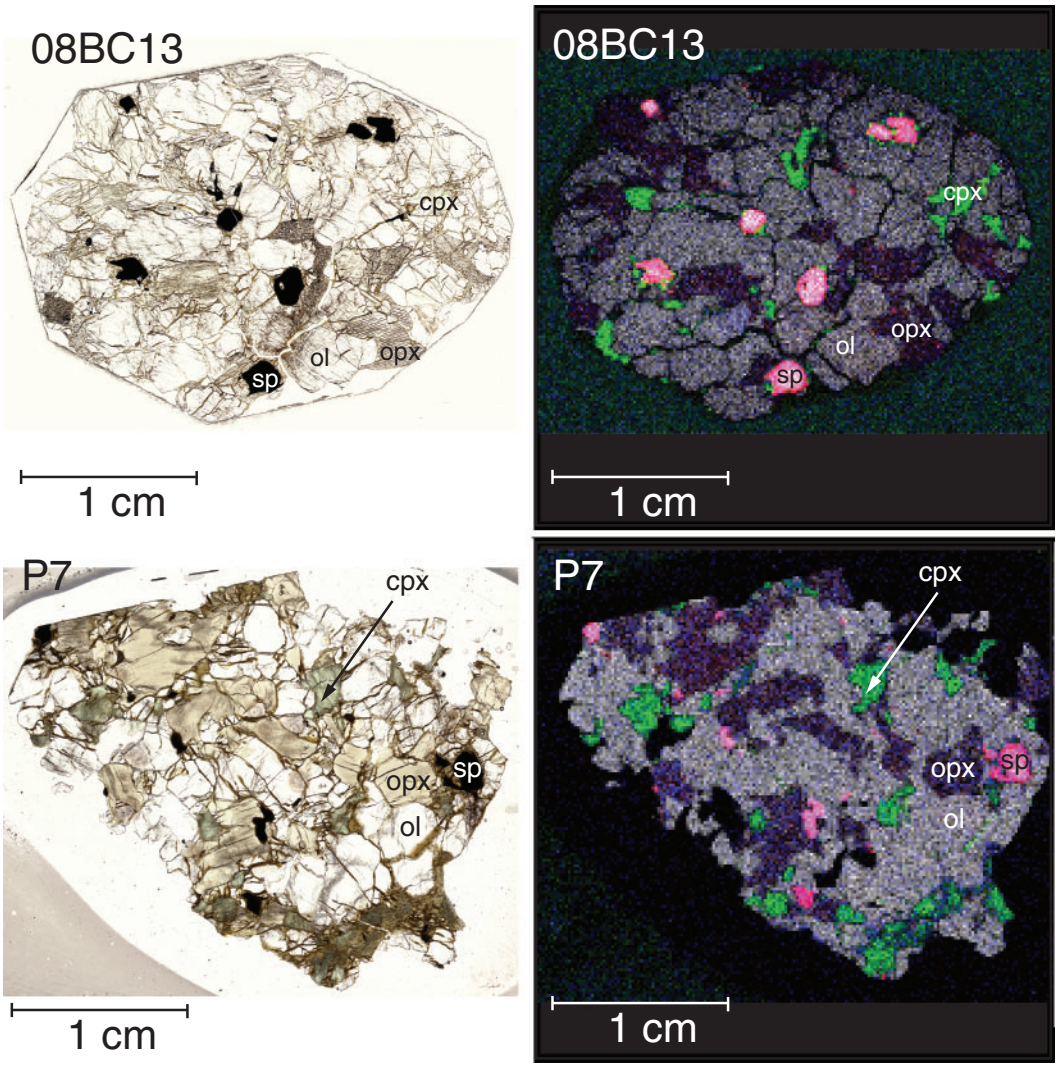

Fig. 3. Petrographic characteristics of two representative Sierran spinel peridotites, 08BC13 and P7. Left column shows a plane-polarized light photograph of a thin section of each peridotite, and the right column shows a μ-XRF map of the same thin section (same orientation). Colors in the μ-XRF maps are as follows: green, Ca; magenta, Cr; dark purple, Al; light purple, Fe. In general, spinel peridotites are coarse-grained, protogranular, and undeformed. Chromian spinels (large opaque grains on left; represented by bright magenta areas in μ-XRF maps at right) tend to be relatively large and euhedral, although P7 shows some deformed spinels.

A ubiquitous feature in the garnet-bearing samples is the presence of garnet coronas around spinels, the latter representing relict spinels from a spinel peridotite protolith.

Garnet microtextures

Garnets in the Sierran peridotite suite mostly occur as coronas rimming spinel or as fine lamellae, ranging in thickness from ~100 nm to 30 μm, in clinopyroxene and orthopyroxene (Fig. 5). Some garnets also occur as discrete grains within the olivine matrix and are unassociated with spinel. Occasionally, discrete garnets cluster along grain boundaries of pyroxenes (see sample 1026 V, Fig. 4) or form loosely disseminated bands that parallel the foliation imposed by diffuse pyroxene bands, such as in peridotites 08BC08 and BC-77 (Fig. 4). Fine-grained opaque kelyphite rims commonly mantle the garnets, although in some cases the garnets have broken down into fine-grained green, aluminous (nearly Cr-free) spinel. These spinels are visually and chemically distinct from the Cr-bearing amber to opaque primary spinels. The kelyphites and green spinels are garnet breakdown products associated with decompression and interaction with the erupting host magma. Other examples of late-stage overprints include thin amphibole lamellae (≤10 μm in width) in the cleavage plane of pyroxenes (Fig. 5). These are most probably due to reaction of pyroxenes with late-stage

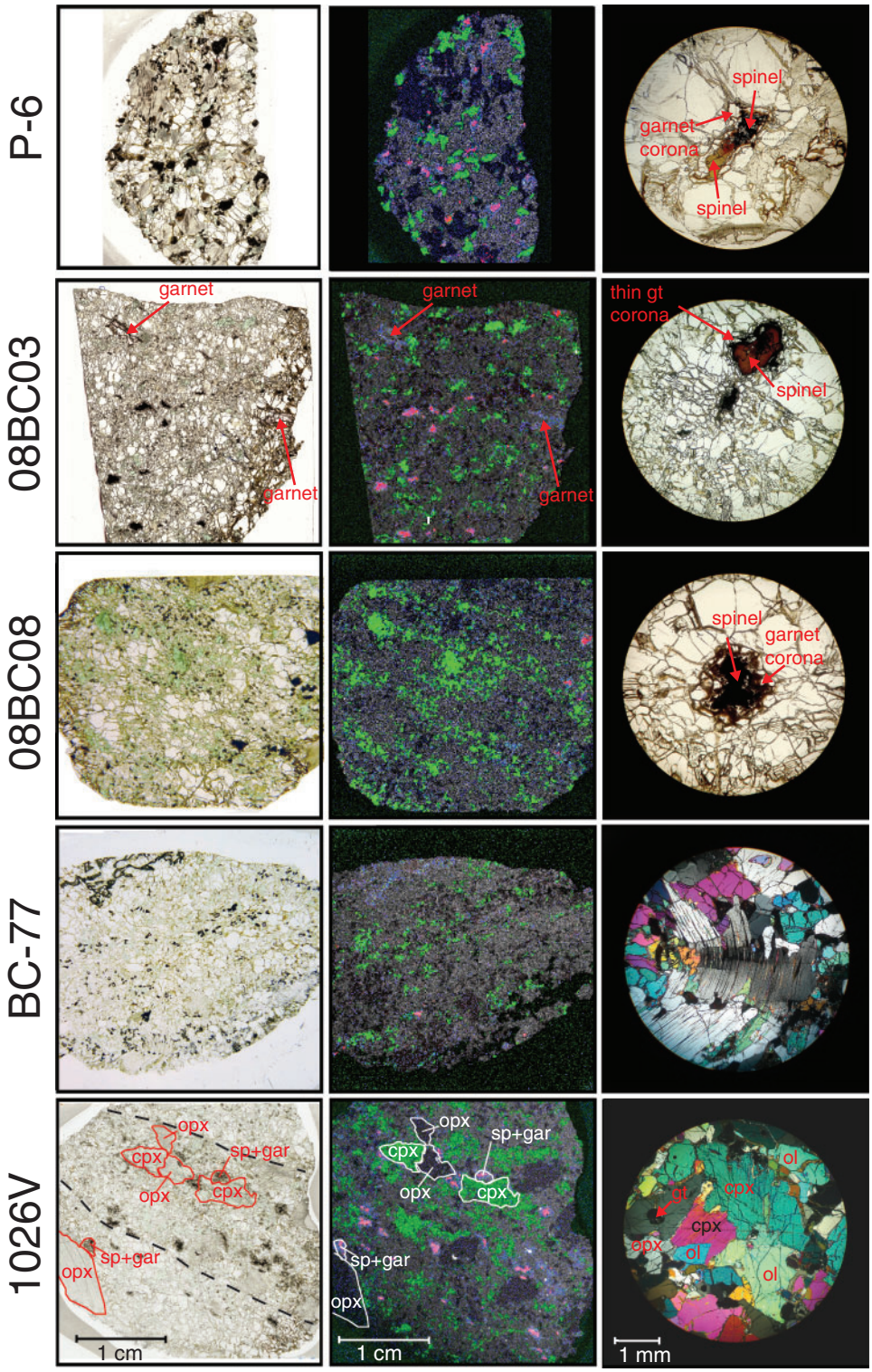

Fig. 4. Petrographic characteristics of five Sierran garnet-bearing spinel peridotite xenoliths: P6, 08BC03, 08BC08, BC-77, 1026 V. Each row corresponds to a single sample (except for P6, see below). The left column shows a plane-polarized light photograph of a 30 μm thin or 200 μm thick section of each sample, the middle column a μ-XRF map of the same thin or thick section in the same orientation as the plane-polarized light photograph, and the right column photomicrographs of the xenoliths. Scale bars shown at the bottom for 1026 V are the same throughout each column. Colors in the μ-XRF maps are the same as in Fig. 3. From top row to bottom row: P6 is characterized by a medium-grained, porphyroclastic texture, with coarser-grained clinopyroxene (compared with the other peridotites) within the weakly foliated bands.

(continued)

fluids that infiltrated along cleavage planes. These late-stage textures, although interesting, are not relevant to our study and thus not discussed any further.

Textural evidence suggests that the garnet lamellae exsolved from their host pyroxenes. This is shown by the presence of Al depletion haloes in the host pyroxene at the contact with the garnet lamellae and, in particular, by a correlation between garnet lamellae thickness and Al depletion halo width (Figs 5 and 6). In Fig. 5, false color WDS EPMA maps of two pyroxene grains containing garnet lamellae in sample 1026 V are shown: pink to red colors indicate high Al (garnet), purple indicates intermediate Al (amphibole), and blue indicates low Al (pyroxene). Bright yellow areas are spinels that probably formed as a result of late-stage garnet breakdown. Two profiles (Lines 2 and 3) from the orthopyroxene in Fig. 5a are plotted in Fig. 6 (garnet and amphibole lamellae are denoted by vertical bars). It can be seen from Fig. 6 that Al depletion haloes are widest next to thick garnet lamellae, and thinner next to thin garnet lamellae. In some cases, thin garnet lamellae appear to have nucleated within the Al-depletion haloes of large garnet lamellae, resulting in shorter wavelength haloes and garnet lamellae superimposed on the longer wavelength haloes associated with the formation of thick garnet lamellae. Al depletion haloes are virtually nonexistent next to amphibole lamellae. The thicknesses of the Al-depletion haloes are limited by diffusion of Al from the pyroxene into the garnet (or amphibole), and thus must relate to the timing of garnet (or amphibole) nucleation and subsequent cooling rate. Thick Al-depletion haloes imply early nucleation whereas thin haloes imply later nucleation. We measured the thicknesses of the Al-depletion haloes and the adjacent garnet lamellae, and found that these show a positive correlation (Fig. 6). This positive correlation strongly suggests that garnet lamellae nucleation and growth is fed by Al diffusing out of the pyroxene. If the garnets were not exsolved, but were of an external (metasomatic) origin, one should not expect any relationship between garnet lamellae thickness and accompanying Al depletion in the host pyroxene. Thus, these observations strongly suggest that the garnet lamellae formed by exsolution from originally high Al orthopyroxene. We note that the lack of Al-depletion haloes around the amphibole lamellae indicates that the amphibole is extraneous to the pyroxene or was so recently nucleated that no time has been allowed for significant Al depletion in the pyroxene, and for these reasons, we ignore the amphibole lamellae from here on.

Spinel microtextures

Cr-spinels within the garnet-bearing spinel peridotites occur as discrete grains, but most are rimmed by garnet coronas. Those spinels mantled by garnet coronas are visibly zoned from deep amber cores to completely opaque rims, the latter characterized by higher Cr content. Zonation is most pronounced in large spinels mantled by thin garnet coronas (see sample 08BC03, Fig. 4). Small spinels mantled by thick garnet coronas are uniformly opaque and show deeply embayed margins (Fig. 4). These observations suggest that large spinels, with high spinel to garnet corona ratios, represent early snapshots of spinel being converted to garnet whereas the small spinels, with lower spinel to garnet corona ratios, represent snapshots in which spinel conversion to garnet has progressed considerably. We note that, within the same samples, some of the spinel–garnet coronas are elongated in shape whereas others are more equidimensional, the former suggesting that spinel to garnet transformation occurred after deformation and the latter suggesting that the transformation occurred during or after deformation. Sample 08BC03 (Fig. 4), for example, contains a spectrum of spinel–garnet textures ranging from large euhedral spinel with incipient garnet coronas to small anhedral spinels with well-developed garnet coronas.

Interpretation of microtextures

Based on the above textural observations, we arrive at the following interpretive sequence of events. The protoliths of the garnet-bearing spinel peridotites were probably

Fig. 4 Continued
Plane-polarized light photograph is of a 200 μm thick section. Olivine and orthopyroxene are also coarse-grained. The photomicrograph shown is actually of sample 08BC04, which is similar in texture to P6 (P6 was available only as a 200 μm thick section). The photomicrograph depicts a relict spinel in the process of transforming into garnet; the light-colored, 'undigested' half represents the original spinel with an incipient, thin garnet corona, whereas the dark-colored, 'digested' half represents increasing degrees of transformation into garnet and thus thicker garnet coronas. 08BC03 is characterized by a fine-grained, porphyroclastic texture. Plane-polarized light photograph is of a 30 μm thin section. Unique to this sample is the presence of large garnet megacrysts, ~5 mm in diameter. 08BC03 also shows transitional spinel–garnet textures, although these are manifested within single spinel–garnet clusters, unlike the transitions observed in P6 and 08BC04. The photomicrograph shows a large, euhedral zoned spinel mantled by a thin garnet corona, and a smaller, anhedral spinel with a thick garnet corona within a few millimeters of each other. 08BC08 is also fine-grained and porphyroclastic, with several large clinopyroxene porphyroclasts containing small garnet grains along the pyroxene grain boundaries. Plane-polarized light photograph of 08BC08 is of a 200 μm thick section, hence the more vivid coloring of the minerals. The photomicrograph shows a well-developed garnet corona around spinel. Plane-polarized light photographs of BC-77 and 1026 V are of 30 μm thin sections. Photomicrograph (crossed nicols) of BC-77 shows a large, heavily deformed orthopyroxene porphyroclast with abundant garnet exsolution lamellae. Bright, thin lamellae are either clinopyroxene or amphibole. Photomicrograph (crossed nicols) of 1026 V shows part of the sample dominated by diffuse bands of loosely dispersed clinopyroxene, with discrete garnet along grain boundaries of clinopyroxene and within the matrix. (Note the absence of deformation in these clinopyroxenes.)

Table 1: Mineral modes and petrography of selected samples

	Spinel peridotites			Garnet-bearing spinel peridotites				
	08BC01	08BC13	P-7	BC77	1026 V	08BC03	08BC04	08BC08
Mode								
Ol	76·65	59·00	53·38	47·00	40·41	46·49	12·25	51·86
Opx	14·06	35·54	31·26	35·45	26·78	25·02	59·46	32·64
Cpx	5·18	4·69	12·96	8·98	20·70	17·71	15·94	7·02
Sp or gt	2·63	1·77	2·80	8·23	11·98	10·28	11·38	8·98
Total	98·51	101·00	100·40	99·66	99·87	99·50	99·03	100·51
$\Sigma(r^2)$	0·36	0·34	0·63	0·20	0·16	0·20	0·36	0·28
Grain size	Medium	Coarse	Coarse	Fine	Fine	Fine	Medium	Fine
Texture	Proto-granular	Proto-granular	Proto-granular	Porphyro-clastic	Porphyroclastic	Porphyroclastic	Transitional	Porphyroclastic
Microtexture	Some recryst. ol	Medium-grained spinels; curv. gb	Medium-grained spinels; curv. gb	Large bent opx porphyrocl. w/ gt lamellae	Distinctive bimodal texture (px, gt-dominated vs recryst. ol dominated)	Large (5 mm) discrete garnets	Trans. spinels similar to 08BC03	Sparse porphyrocl.
				Garnet coronas around spinel rare	Large bent opx porphyrocl. w/ gt lamellae; garnet coronas around spinel abundant	Transitional spinel types grading from equidimensional w/ thin gt corona to embayed w/ thick gt corona	Very px-rich; Poikilitic opx and cpx enclosing olivine	Abundant foliation defined by diffuse cpx and discrete garnets; highly recryst. Ol matrix

Ol, olivine; Opx, orthopyroxene; Cpx, clinopyroxene; Sp, spinel; Gt, garnet. Proto., protogranular; Porphyro., porphyroclastic; Trans., transitional between protogranular and porphyroclastic; recryst., recrystallized; curv., curvilinear; gb, grain boundary; porphyrocl., porphyroclast; px, pyroxene. $\Sigma(r^2)$ = sum of residuals squared (modes were determined using least-squares regression of average mineral chemistries and whole-rock compositions). Grain size defined as follows: fine grained, $\leq$1 mm; medium grained, 1–4 mm; coarse grained, $\geq$4 mm. For porphyroclastic samples, grain size refers to that of the matrix.

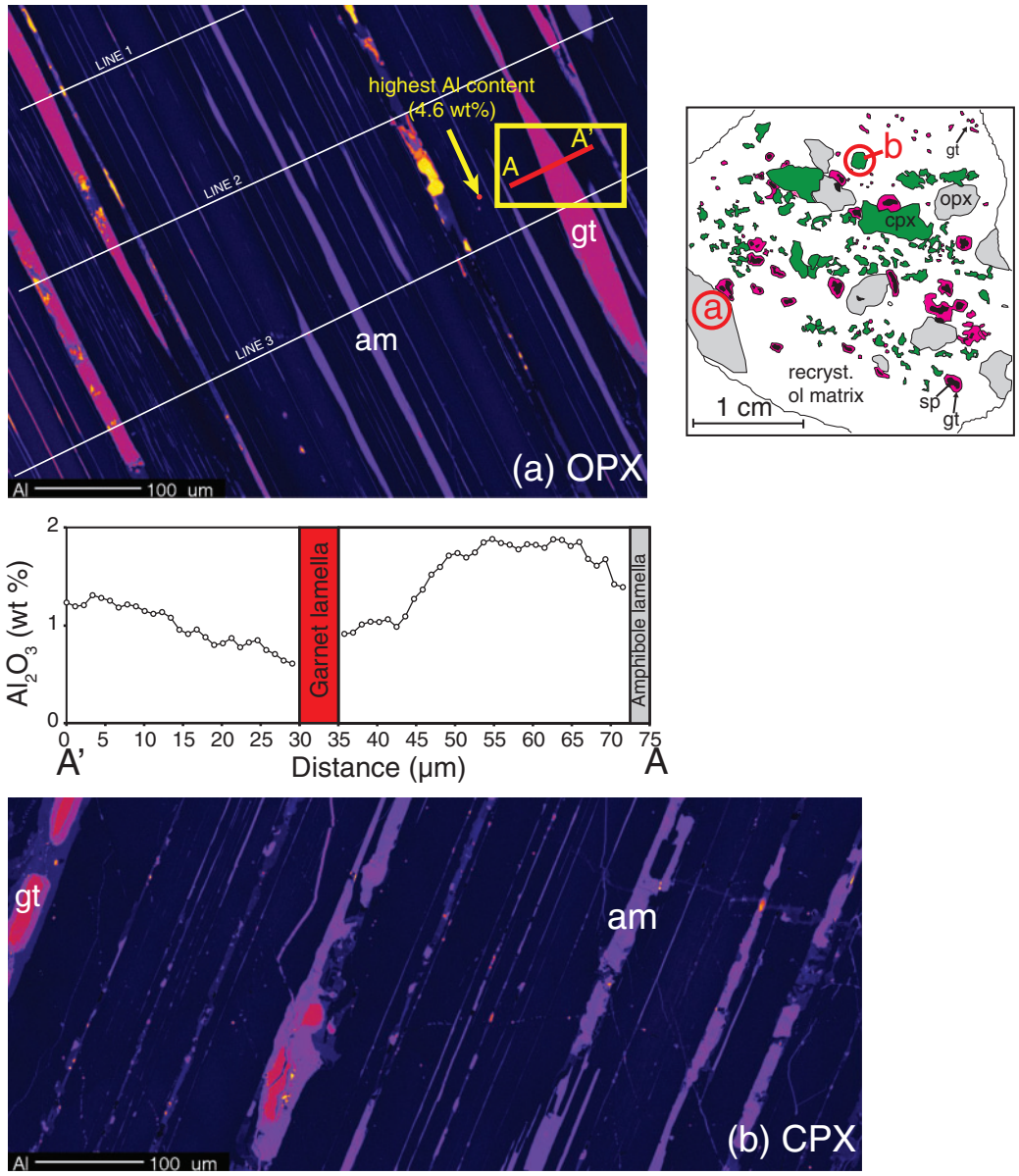

Fig. 5. WDS (wavelength-dispersive EPMA) false-color maps of Al content in orthopyroxene (a) and clinopyroxene (b) in sample 1026 V. Inset shows index map of 1026 V with the grains that were analyzed in (a) and (b). Warm colors (pink, red) represent high Al (i.e. garnet); cool colors (purple, blue) represent low Al (i.e. amphibole, pyroxene). Quantitative WDS points along transect A–A' are plotted in the profile below the opx map. Each point on the transect represents a 1 μm spot analysis. am, amphibole; gt, garnet.

coarse-grained protogranular spinel peridotites. These peridotites were subsequently deformed, leading to the formation of porphyroclastic textures characterized by fine-grained recrystallized olivines and large, deformed orthopyroxene porphyroclasts, the latter representing relicts of the original undeformed spinel peridotite protolith. Deformation has been coincident with or followed by the formation of garnet lamellae in pyroxenes and garnet coronas around spinels. Garnet formation in pyroxenes is most probably due to exsolution from high-Al pyroxenes (typical of spinel peridotites), as exemplified by the Al-depletion haloes in the pyroxenes. The elongated shape of some spinels and spinel–garnet coronas suggests that metamorphism was concomitant with deformation. That some spinel–garnet coronas are circular also suggests that metamorphic transformation from spinel to garnet may have continued after deformation ceased. Diffuse bands of disseminated clinopyroxene and garnet grains

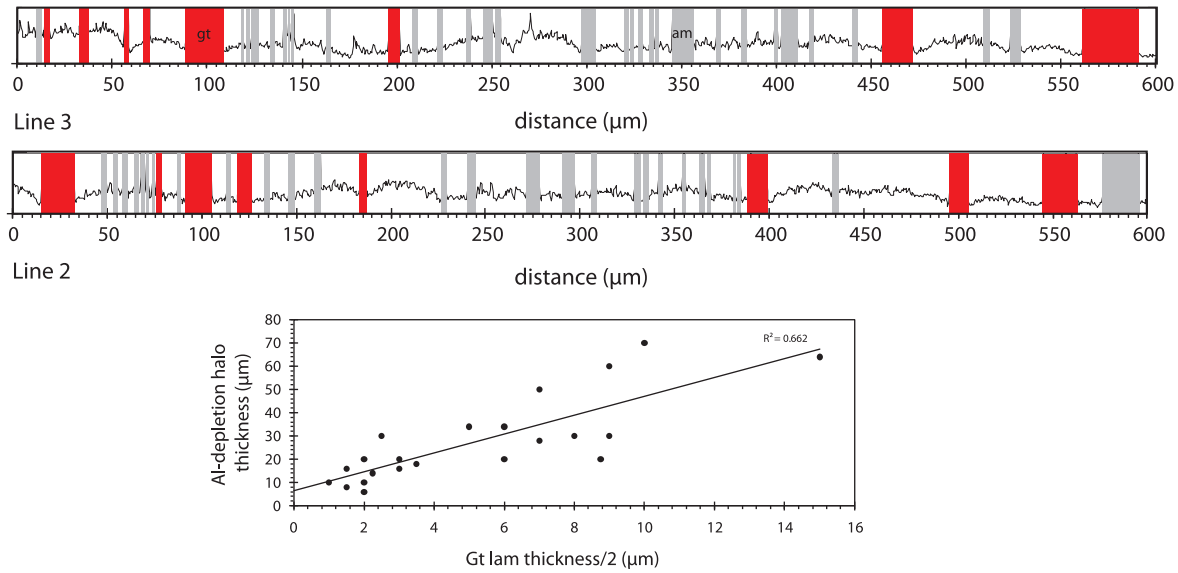

Fig. 6. Top profiles of Al relative intensity vs distance for two transects shown in Fig. 5a. Shaded rectangles represent garnet (gt) and amphibole (am) lamellae. Bottom: plot of Al depletion halo thickness vs half-thickness of garnet lamellae.

suggest open-system behavior owing to infiltration of refertilizing silicate melts (to be discussed below). These clinopyroxene-rich bands follow the shape-preferred orientation of recrystallized olivines, suggesting introduction during deformation.

Whole-rock chemistry

Whole-rock major and trace element data for spinel peridotites and garnet-bearing spinel peridotites are reported in Tables 2 and 3, respectively; oxide variation diagrams are shown in Fig. 7. Whole-rock trace element data for samples P-7, P-10, BC98-2, 1026 V, and BC-77 were previously reported by Lee (2005). Samples 1026 V and BC-77 were previously investigated by Lee *et al.* (2001) and Lee (2005). Samples 08BC14 and 08BC07 were not extensively analyzed owing to pervasive serpentinization, but we report whole-rock XRF and selected mineral data for these samples for completeness. Here, we present new whole-rock and *in situ* geochemical data allowing us to constrain a more detailed P–T path for these xenoliths.

In terms of whole-rock major elements, the Sierran xenoliths range from depleted spinel peridotites to fertile garnet-bearing spinel peridotites. Mg-numbers [atomic Mg/(Mg + Fe) × 100] range from 86 to 91. This range overlaps that of typical residual peridotites, but values lower than 89 indicate that some of the peridotites are more fertile than canonical primitive mantle [see McDonough & Sun (1995) and Walter (1998) and references therein]. CaO, Na_2O, and Al_2O_3, measures of fertility, correlate negatively with Mg-number and MgO, with the spinel peridotites characterized by generally high Mg-number and low CaO, Na_2O, and Al_2O_3 (depleted) and the garnet-bearing spinel peridotites characterized by high and variable CaO, Na_2O and Al_2O_3 and low Mg-number (fertile). However, overlap in major element trends between spinel and garnet-bearing spinel peridotites indicates that the Sierran peridotites define a compositional continuum, with some garnet-bearing spinel peridotites preserving depleted signatures.

The most depleted garnet-bearing spinel peridotites, exemplified by BC-77 and 08BC07, have CaO and Al_2O_3 contents as low as 2·2 and 1·08 wt %, respectively, overlapping the CaO and Al_2O_3 contents of some spinel peridotites from the same location. However, the most fertile garnet-bearing peridotites (1026 V, 08BC04) have >4 wt % CaO and >4 wt % Al_2O_3, higher than that of canonical primitive mantle (3·55 wt % CaO and 4·45 wt % Al_2O_3; McDonough & Sun, 1995). Although the sense of these compositional trends is broadly consistent with that expected for melt depletion, the trends do not all pass through primitive mantle values as would be expected if these trends were imparted solely by melt depletion of a homogeneous primitive mantle source. In the plot of CaO vs Al_2O_3 (Fig. 7a), many garnet-bearing spinel peridotites 'fan out' in an array towards higher CaO and Al_2O_3, but in terms of MgO vs Al_2O_3, these peridotites are just as depleted as spinel peridotites. High CaO is associated with those samples with abundant diffuse clinopyroxene

Table 2: Whole-Rock Major Element Compositions

	Spinel Peridotites					
	08BC02 serpentinized	08BC06	08BC13	P-7*	P-10*	BC98-2*
XRF						
SiO_2	45·01	48·09	45·72	45·45	48·97	46·18
TiO_2	0·042	0·028	0·011	0·092	0·051	0·030
Al_2O_3	2·11	1·63	1·50	3·42	1·99	3·18
FeOT	8·35	7·78	7·83	8·23	8·01	7·65
MnO	0·14	0·26	0·13	0·14	0·21	0·14
MgO	42·45	38·61	43·51	39·24	38·16	40·01
CaO	1·48	3·48	1·25	3·14	2·36	2·49
Na_2O	0·21	0·08	0·04	0·28	0·17	0·21
K_2O	0·14	0·03	0·01	0·01	0·05	0·09
P_2O_5	0·066	0·016	0·011	0·010	0·010	0·020
Total	100	100	100	100	100	100
Difference	1·82	4·15	2·01	1·02	1·19	0·62
Mg#	0·90	0·90	0·91	0·89	0·89	0·90
MR-ICPMS						
TiO_2				0·09	0·05	0·03
Al_2O_3				2·98	1·67	2·63
FeOT				8·25	7·94	7·41
MnO				0·13	0·20	0·13
MgO						
CaO						
Na_2O						
K_2O						
P_2O_5				0·00835	0·00631	0·0175

	Garnet-bearing Spinel Peridotites									
	BC77*	1026V*	P-1**	P-6	96D-18	08BC03	08BC04	08BC08	08BC14 serpentinized	08BC07 serpentinized
XRF										
SiO_2	47·55	47·95	45·30	45·84	48·46	46·84	50·95	46·86	50·02	47·07
TiO_2	0·031	0·031	0·122	0·142	0·152	0·064	0·189	0·023	0·070	0·031
Al_2O_3	2·60	3·59	2·78	4·21	6·63	3·17	4·83	2·44	3·30	1·87
FeOT	7·54	7·08	8·93	8·26	7·61	7·72	8·10	7·77	7·75	7·69
MnO	0·14	0·15	0·15	0·13	0·15	0·25	0·12	0·13	0·61	0·16
MgO	39·17	35·48	37·62	37·41	33·14	37·15	31·19	40·43	25·96	42·03
CaO	2·76	5·40	4·81	3·61	3·45	4·58	3·99	2·17	11·95	1·08
Na_2O	0·19	0·28	0·29	0·35	0·35	0·13	0·48	0·11	0·18	0·03
K_2O	0·02	0·04	0·01	0·03	0·05	0·06	0·11	0·04	0·13	0·03
P_2O_5	0	0	0	0·010	0·010	0·025	0·034	0·015	0·027	0·016
Total	100	100	100	100	100	100	100	100	100	100
Difference	1·00	1·44	0·84	0·60	0·79	4·21	3·72	1·90	13·98	2·79
Mg#	90·3	89·9	88·3	89·0	88·6	89·6	87·3	90·3	85·7	90·7
MR-ICPMS										
TiO_2	0·03	0·03				0·04	0·15	0·02	0·05	
Al_2O_3	2·29	2·96				2·81	3·96	2·06	2·53	
FeOT	7·75	7·01				6·74	6·86	6·98	6·20	
MnO	0·14	0·14				0·23	0·11	0·13	0·53	
MgO						33·03	27·29	36·02	20·92	
CaO						3·97	3·36	1·85	9·60	
Na_2O						0·12	0·43	0·11	0·16	
K_2O						0·05	0·10	0·04	0·11	
P_2O_5	0·00529	0·00138				0·00704	0·0158	0·003	0·0168	
Mg#						89·7	87·6	90·2	85·7	

Difference = Normalized XRF total (100% volatile-free basis) - Unnormalized XRF total
Mg# = (atomic $Mg/(Mg + Fe_T) \times 100$)
*MR-ICPMS data from Lee (2005)
**From Dodge et al., 1988

Table 3: Whole-rock trace element geochemistry (values in ppm)

		Spinel peridotites					
		08BC02	08BC06	08BC13	P-7*	P-10*	BC98-2*
Li	LR-ICPMS				3·5	19·1	7·2
Sc	MR-ICPMS				12·9	6·8	10·7
	XRF	8	9	10			
Ti	MR-ICPMS				514	305	192
	XRF	246	162	66			
V	MR-ICPMS				59·2	36·6	43·0
	XRF	36	42	45			
Cr	XRF	2358	2751	2954			
Co	MR-ICPMS				112	116	109
Ni	MR-ICPMS				2415	2490	2504
	XRF	2405	2072	2210			
Cu	MR-ICPMS				24·8	1·95	1·26
	XRF	14	24	12			
Zn	MR-ICPMS				44·4		48·6
	XRF	46	48	49			
Ga	LR-ICPMS				2·95	1·94	2·59
	XRF	3	3	2			
Rb	LR-ICPMS				1·20	5·89	5·05
	XRF	9	2	0			
Sr	LR-ICPMS				20·7	58·9	61·3
	XRF	52	41	17			
Y	LR-ICPMS				2·34	0·677	1·18
	XRF	3	2	1			
Zr	LR-ICPMS				4·40	1·75	5·90
	XRF	13	3	2			
Nb	LR-ICPMS				0·061	0·060	0·364
Cs	LR-ICPMS				1·09	5·13	2·73
Ba	LR-ICPMS				9·2	18·6	44·5
	XRF	51	30	21			
La	LR-ICPMS				0·201	0·384	1·14
Ce	LR-ICPMS				0·559	0·411	2·15
Pr	LR-ICPMS				0·105	0·0556	0·295
Nd	LR-ICPMS				0·589	0·254	1·21
Sm	LR-ICPMS				0·211	0·0700	0·234
Eu	LR-ICPMS				0·0855	0·0318	0·0784
Gd	LR-ICPMS				0·284	0·0883	0·216
Tb	LR-ICPMS				0·0531	0·0151	0·0324
Dy	LR-ICPMS				0·367	0·0918	0·188
Ho	LR-ICPMS				0·0887	0·0211	0·0425
Er	LR-ICPMS				0·275	0·0631	0·139
Tm	LR-ICPMS				0·0419	0·0098	0·0231
Yb	LR-ICPMS				0·260	0·0679	0·159
Lu	LR-ICPMS				0·0401	0·0109	0·0262
Hf	LR-ICPMS				0·127	0·0501	0·156
Ta	LR-ICPMS				0·0044	0·0021	0·0216
Tl	LR-ICPMS				0·0794	0·0595	0·0857
Pb	LR-ICPMS				0·227	0·507	0·794
Th	LR-ICPMS				0·0337	0·041	0·412
U	LR-ICPMS				0·0167	0·0626	0·211

(continued)

Table 3: Continued

		Garnet-bearing spinel peridotites						
		BC77*	1026 V*	08BC03	08BC04	08BC08	08BC14 (serp.)	08BC07
Li	LR-ICPMS	23·9	14·0	18·8	37·0	10·3	59·5	
Be	LR-ICPMS			0·111	0·105		0·414	
Sc	MR-ICPMS	8·98	17·6	15·9	16·6	12·1	12·8	
	XRF			14	17	13	14	9
Ti	MR-ICPMS	164	159	287	963	104	327	
	XRF	186	186	372	1091	132	360	180
V	MR-ICPMS	62·5	86·6	66·7	84·6	52·4	74·9	
	XRF			67	92	58	79	33
Cr	XRF			2788	2770	2879	3506	2621
Co	MR-ICPMS	111	100	119	113	112	135	
Ni	MR-ICPMS	2406	2297	2505	2360	2380	2699	
	XRF			2124	1976	2182	2249	2348
Cu	MR-ICPMS	1·1	43·8	24·3	26·6	23·1	37·1	
	XRF			28	30	26	44	7
Zn	MR-ICPMS	49·6	50·2	29·1	33·2	29·2	30·6	
	XRF			42	57	45	58	48
Ga	LR-ICPMS	2·02	2·28	2·12	3·61	1·80	2·63	
	XRF			5	5	4	2	2
Rb	LR-ICPMS	2·02	2·58	4·98	13·1	2·19	14·2	
	XRF			5	13	2	13	2
Sr	LR-ICPMS	16·5	33·2	60·8	45·4	15·4	335	
	XRF			67	51	19	324	30
Y	LR-ICPMS	0·571	2·17	3·77	3·51	0·901	4·30	
	XRF			5	5	2	4	2
Zr	LR-ICPMS	4·39	4·46	3·61	9·54	0·632	3·44	
	XRF			10	12	2	5	2
Nb	LR-ICPMS	0·043	0·066	0·184	0·153	0·051	0·209	
	XRF			2	1	1	1	1
Cs	LR-ICPMS	1·67	2·85	3·77	6·28	1·78	12·6	
Ba	LR-ICPMS	16·9	9·8	57·5	50	20·4	112	
	XRF			64	53	29	111	44
La	LR-ICPMS	0·245	0·228	0·863	0·758	0·115	2·41	
Ce	LR-ICPMS	0·85	0·877	1·26	1·58	0·232	2·53	
Pr	LR-ICPMS	0·076	0·068	0·165	0·258	0·03	0·294	
Nd	LR-ICPMS	0·317	0·315	0·741	1·37	0·137	1·27	
Sm	LR-ICPMS	0·0599	0·100	0·203	0·439	0·0471	0·296	
Eu	LR-ICPMS	0·0233	0·0417					
Gd	LR-ICPMS	0·0741	0·160	0·282	0·499	0·0651	0·425	
Tb	LR-ICPMS	0·0121	0·0323	0·0580	0·0924	0·0154	0·0655	
Dy	LR-ICPMS	0·103	0·295	0·452	0·590	0·121	0·434	
Ho	LR-ICPMS	0·0172	0·0767	0·122	0·131	0·0321	0·106	
Er	LR-ICPMS	0·0465	0·259	0·414	0·379	0·109	0·337	
Tm	LR-ICPMS	0·007	0·0422	0·0671	0·0561	0·0185	0·0505	
Yb	LR-ICPMS	0·0420	0·273	0·440	0·355	0·123	0·319	
Lu	LR-ICPMS	0·0063	0·0427	0·0696	0·0533	0·0203	0·0521	
Hf	LR-ICPMS	0·11	0·104	0·111	0·283	0·0196	0·116	
Ta	LR-ICPMS	0·0023	0·0038	0·0093	0·0117	0·0031	0·0110	
Tl	LR-ICPMS	0·0624	0·129	0·193	0·351	0·129	0·291	
Pb	LR-ICPMS	0·236	0·603	0·214	1·12	0·155	0·664	
Th	LR-ICPMS	0·0077	0·0087	0·181	0·175	0·0126	0·157	
U	LR-ICPMS	0·0108	0·0071	1·03	0·0821	0·0158	2·98	

*MR- and LR-ICPMS data from Lee (2005); XRF data this study.
MR-ICPMS: medium resolution ($m/\Delta m = 3000$). LR-ICPMS: low resolution ($m/\Delta m = 300$).

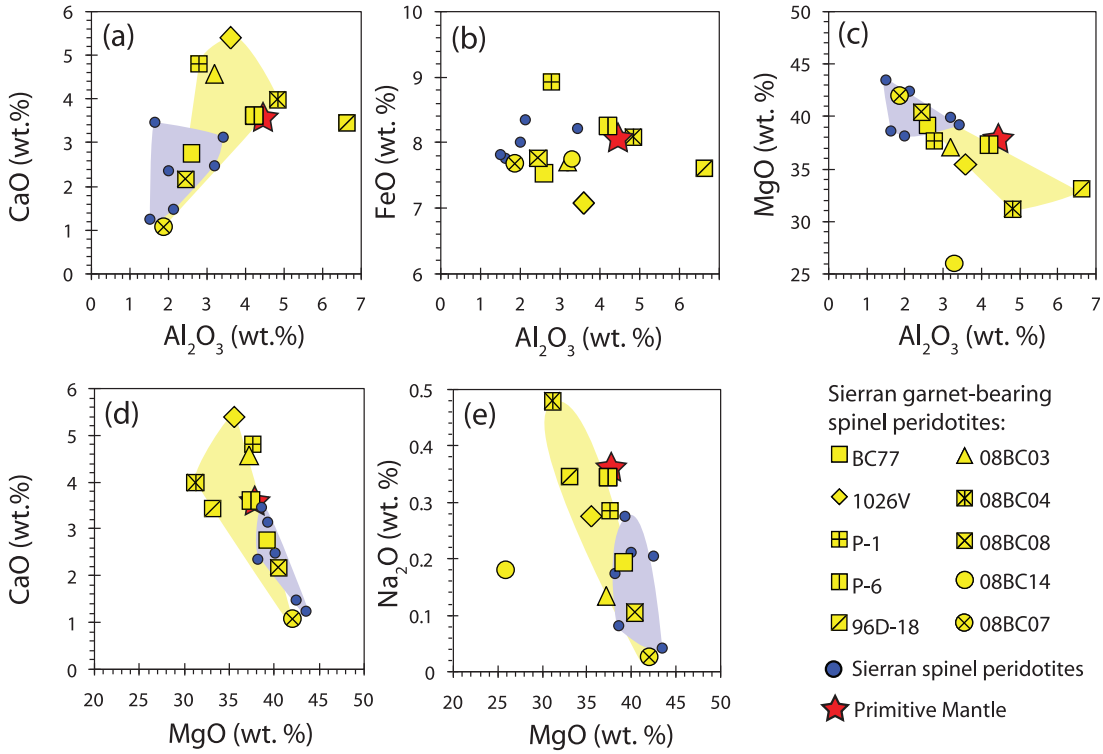

Fig. 7. Whole-rock major element variation diagrams showing the relationship between spinel peridotites and garnet-bearing spinel peridotites. The former are typically depleted in terms of major elements; the latter are comparatively more fertile, although some garnet-bearing peridotites overlap the spinel peridotites. Sample 08BCl4 is not shown in (a) and (e) because of its anomalous CaO (11 wt %). 08BCl4 is highly serpentinized and altered, which is reflected in its low XRF total (see Table 2). (a) CaO vs Al_2O_3; (b) FeO vs Al_2O_3; (c) MgO vs Al_2O_3; (d) CaO vs MgO; (e) Na_2O vs MgO.

bands. Finally, the relatively linear trend shown by Na_2O vs MgO suggests a mixing between depleted peridotite and a melt rather than simple melt depletion. This is because Na_2O, which is highly incompatible, should show a non-linear melt-depletion trend when plotted against highly compatible elements such as MgO. Collectively, these textural, and major and minor element trends suggest that these samples have been refertilized.

The lack of a simple melt-depletion history is also evident from the trace element systematics (Fig. 8). Whole-rock Yb contents span a wide range within the suite of garnet-bearing spinel peridotites, with some samples (1026 V, 08BC03, 08BCl4) as fertile as primitive mantle (>0·4 ppm Yb), whereas other samples (BC-77, 08BC08) are highly depleted in Yb (<0·05 ppm Yb) and hence resemble the depleted spinel peridotites in terms of Yb. In contrast, in most samples, whole-rock Ti contents are depleted (<600 ppm) compared with primitive mantle (1205 ppm Ti), with the exception of samples P-l, P-6, and 08BC04, which have whole-rock Ti >600 ppm. Because Ti and Yb are both considered moderately incompatible elements, a positive correlation between Ti and Yb would be expected for a simple melt-depletion trend. Instead, we observe a general decoupling between Ti and Yb (Fig. 8a): most garnet-bearing spinel peridotites plot within a relatively restricted range of Ti, but show a wide range in Yb. The fact that Yb correlates with Al_2O_3 indicates that the same processes that imparted variations in major element composition have also imparted variations in Yb, but not in Ti.

Whole-rock trace element variation diagrams are shown in Fig. 9, with the elements listed in approximate order of increasing compatibility during partial melting of anhydrous peridotitic mantle (Hofmann, 1988). The overall trace element patterns [normalized to the primitive mantle values of McDonough & Sun (1995)] indicate whole-rock enrichments in fluid-mobile elements (Cs, Ba, Rb, Sr, La) and depletions in high field strength elements (HFSE; Nb, Ta). If only REE are plotted (not shown), the spinel peridotites have generally flat REE patterns with a slight increase in the light REE (LREE). In contrast, many garnet-bearing spinel peridotites (08BC03, 08BC08, 1026 V) have gently concave-upwards REE patterns, with

middle REE (MREE) depleted relative to LREE and heavy REE (HREE).

Mineral chemistry

Orthopyroxene

Major element compositions of orthopyroxenes in spinel peridotites and garnet-bearing spinel peridotites are reported in Table 4. Trace element compositions of orthopyroxenes in garnet-bearing spinel peridotite 1026 V are reported in Table 5. Orthopyroxenes in the Sierran xenoliths are enstatite-rich, with Mg-number between 90 and 92. Rims of orthopyroxene generally have slightly higher Mg-number than corresponding cores. In addition, Al_2O_3 in cores is several weight per cent higher than in rims. As illustrated in Fig. 5a, there is a strong decrease in Al_2O_3 from areas in orthopyroxene without exsolved garnet ('core' areas) towards the interface with exsolved garnet ('rim' areas); for example, Al_2O_3 is ~4·6 wt % in the core and decreases to 0·7 wt % at the garnet–orthopyroxene interface. Cr_2O_3 contents were found to be high in the cores and low on the rims (Table 4). Primitive-mantle normalized REE concentrations in orthopyroxene from sample 1026 V are shown in Fig. 10a. Two measurements of orthopyroxene show increasing HREE concentrations but this may be due to contamination during analysis from a nearby garnet lamella.

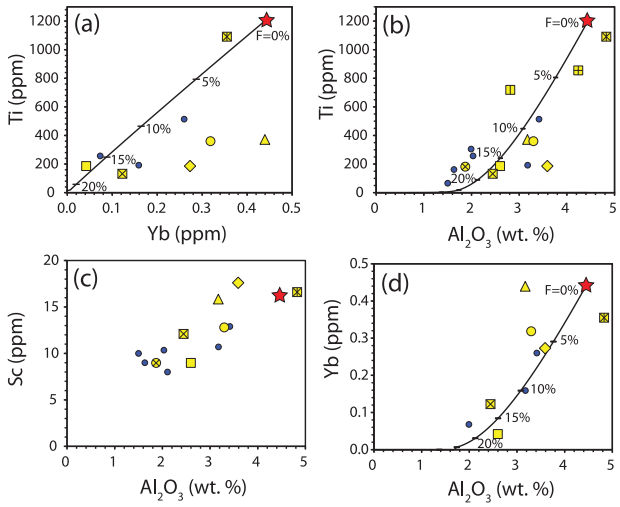

Fig. 8. Whole-rock trace element and major element variations for spinel peridotites and garnet-bearing spinel peridotites. Continuous black lines with tick marks represent hypothetical melting trends (see text for details) starting from primitive mantle (McDonough & Sun, 1995). Symbols as in Fig. 7. (a) Ti vs Yb; (b) Ti vs Al_2O_3; (c) Sc vs Al_2O_3; (d) Yb vs Al_2O_3.

Clinopyroxene

Major element compositions of clinopyroxene in both spinel peridotites and garnet-bearing spinel peridotites are presented in Table 6. The trace element geochemistry of clinopyroxenes in selected garnet-bearing spinel peridotites is reported in Table 5. Clinopyroxenes are Cr-diopsides (average Cr_2O_3 0·9 wt %). Cores are higher in Al_2O_3 than rims; for example, sample 08BC03 has clinopyroxene cores with 3·1 wt % Al_2O_3 decreasing to 1·8 wt % at the rim.

Plots of Gd vs Yb in clinopyroxene and garnet located along grain boundaries of clinopyroxene or within close

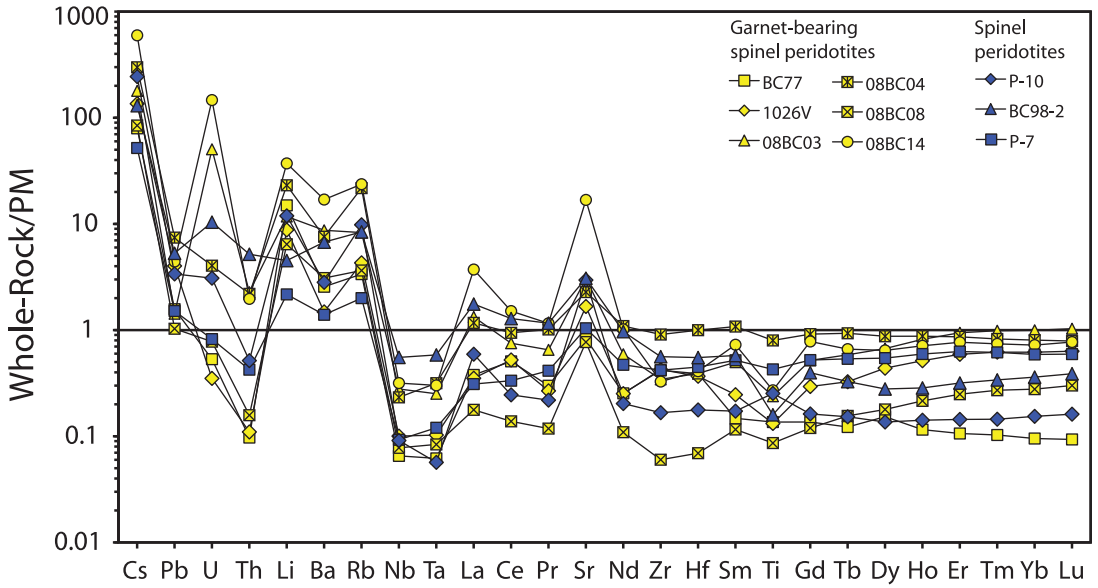

Fig. 9. Whole-rock trace element patterns of spinel peridotites and garnet-bearing spinel peridotites, normalized to primitive mantle values (McDonough & Sun, 1995).

Table 4: Orthopyroxene major element compositions

	Spinel peridotites								
	08BC01		08BC06	08BC13		P-7		P-10	BC98-2
	Rim	Core	Core	Rim	Core	Rim	Core	Core	Core
SiO_2	54·77	54·98	54·07	54·20	54·14	54·85	54·84	55·93	57·51
TiO_2	0·09	0·06	0·05	0·02	0·02	0·07	0·09	0·07	0·02
Al_2O_3	3·46	3·40	4·00	2·81	3·34	3·69	4·21	2·66	0·76
Cr_2O_3	0·63	0·61	0·76	0·50	0·66	0·40	0·48	0·44	0·14
FeO	4·61	4·72	5·87	5·89	5·64	6·50	6·42	6·05	5·53
MnO	0·10	0·12	0·13	0·13	0·14	0·16	0·16	0·15	0·11
MgO	35·43	35·92	34·52	35·38	35·26	33·86	33·34	34·57	36·10
CaO	0·87	0·20	0·30	0·28	0·21	0·19	0·55	0·26	0·12
Na_2O	0·04	0·02	0·02	0·00	0·03	0·00	0·03	0·01	0·02
K_2O	0·00	0·00	0·01	0·00	0·00				
Total	99·99	100·04	99·72	99·19	99·43	99·72	100·12	100·14	100·31
Mg-no.	93·19	93·13	91·30	91·47	91·76	90·28	90·25	91·06	92·09

	Garnet-bearing spinel peridotites													
	1026 V				BC-77		08BC-03		08BC-04		08BC-08		08BC-14	
	Rim of large opx	Core of large opx	Rim of small opx	Core of small opx	Rim	Core	Rim	Core	Rim	Core	Rim	Core	Rim	Core
SiO_2	57·19	55·13	57·06	56·26	56·87	54·98	56·62	56·16	55·35	53·77	56·21	55·29	54·87	53·81
TiO_2	0·04	0·04	0·02	0·02	0·03	0·03	0·04	0·10	0·13	0·08	0·03	0·03	0·06	0·05
Al_2O_3	0·61	4·58	1·35	2·61	0·78	3·58	0·70	1·46	2·08	4·77	0·75	2·15	2·61	4·34
Cr_2O_3	0·04	0·60	0·41	0·59	0·21	0·71	0·16	0·31	0·22	0·30	0·22	0·53	0·73	0·61
FeO	5·80	6·23	6·19	5·76	5·51	5·83	5·46	5·44	6·45	6·70	6·01	5·95	5·39	5·40
MnO	0·14	0·21	0·13	0·17	0·12	0·11	0·11	0·12	0·10	0·12	0·13	0·14	0·10	0·10
MgO	35·43	32·85	35·17	34·71	36·12	34·18	36·24	35·82	35·00	33·95	36·52	35·38	35·32	34·57
CaO	0·12	0·11	0·17	0·16	0·11	0·15	0·15	0·38	0·30	0·22	0·17	0·14	0·17	0·21
Na_2O	0·01	0·03	0·02	0·00	0·02	0·01	0·03	0·04	0·03	0·02	0·01	0·02	0·02	0·03
K_2O	0·02	0·01	0·01	0·00	0·00		0·00	0·00	0·00	0·00	0·01	0·01	0·00	0·00
Total	99·41	99·78	100·52	100·26	99·77	99·58	99·52	99·81	99·66	99·92	100·05	99·64	99·26	99·13
Mg-no.	91·59	90·38	91·01	91·49	92·12	91·27	92·21	92·15	90·63	90·04	91·55	91·38	92·12	91·94

Rims and cores reported below are of the same mineral grain; each column represents a single spot analysis.

proximity to clinopyroxene are shown in Fig. 11. These plots show that garnet formation in clinopyroxene causes the clinopyroxene host and complementary garnet to evolve away from each other in Gd–Yb space. In particular, clinopyroxenes initially have high Yb, but with progressive equilibration with garnet, Yb becomes depleted. Combined with the Al-depletion haloes in clinopyroxene adjacent to garnet (see above), these observations are consistent with the suggestion that these clinopyroxenes initially had high Al and Yb contents and thus formed initially in a garnet-free environment. Their present Al- and Yb-depleted compositions result from subsolidus equilibration with garnet, most probably generated by direct exsolution from the pyroxenes.Primitive

Table 5: Trace element compositions of pyroxenes

	Orthopyroxene trace element compositions (ppm) in sample 1026V					Representative clinopyroxene trace element concentrations (ppm) in selected garnet-bearing spinel peridotites				
	1026V	1026V	1026V	1026V	1026V	1026V	BC77		08BC03	08BC08
	R2-10	R2-11	R3-017	R3-021	R3-023	Porphyrocl. w/ gt lam.	18-cpx (rim)	24-cpx (rim)	Large porphyrocl.	Large porphyrocl. w/ gt on grain boundary
Li	2·44	139	2·03	3·07	2·26	5·18	1·16	0·78	3·00	1·94
Ti	120	108	152	126	135	254	454	319	1378	275
Co	62·5	71·5	58·1	48·5	61·0	16·6	23·3	18·5	17·2	18·0
Ni	788	760	734	745	736	260	284	199	288	335
Zn									7·81	9·06
Rb	0·100	1·49	0·124	0·036	0·028	0·610	0·031	0·028	0·123	0·134
Sr	0·038	0·930	1·77	0·645	0·042	100	62·7	49·7	59·6	105
Y	0·189	0·299	0·051	0·030	0·013	0·782	0·197	0·125	1·12	0·419
Zr	1·21	0·788	0·695	0·357	0·241	1·86	6·39	5·14	10·0	1·08
Nb	0·080	0·093	0·162	0·136	0·061	0·115	0·725	0·504	0·062	0·034
Cs	0·017	4·21	0·003	0·002	0·0004	1·20	0·0004	0·005	0·017	0·011
Ba	1·79	0·814	0·893	0·392	0·174	7·84	0·155	0·187	6·03	1·03
La	0·011	0·066	0·035	0·014	0·0020	0·906	1·09	0·871	1·32	0·868
Ce	0·036	0·095	0·092	0·037	0·0037	2·03	4·43	3·91	3·58	2·24
Pr	0·0032	0·0056	0·0094	0·0043	0·0008	0·228	0·556	0·488	0·557	0·258
Nd	0·045		0·031	0·015		0·955	2·14	1·71	3·08	1·08
Sm	0·013		0·018	0·011	0·0063	0·262	0·378	0·271	1·00	0·289
Eu	0·0083		0·002	0·0017	0·0020	0·094	0·099	0·072	0·323	0·088
Gd	0·011	0·033	0·014	0·0093	0·0022	0·332	0·352	0·205	0·874	0·232
Tb			0·0028	0·00086	0·0012	0·045	0·044	0·028	0·100	0·028
Dy	0·023	0·025	0·0082	0·010	0·0049	0·227	0·166	0·106	0·447	0·150
Ho	0·0064	0·018	0·0012	0·0014	0·0012	0·031	0·019	0·0072	0·050	0·021
Er	0·036	0·034	0·0067	0·0042	0·0039	0·051	0·019	0·013	0·087	0·039
Tm									0·013	0·0085
Yb	0·031	0·042	0·008	0·0043	0·0043	0·043	0·0048	0·0082	0·042	0·033
Lu	0·012	0·0034	0·00043		0·0011	0·0084			0·004	0·006
Hf	0·028	0·054	0·013	0·0054	0·0068	0·121	0·244	0·183	0·545	0·111
Ta	0·0032	0·0011	0·0020	0·0027	0·0012				0·020	0·011
Pb	0·175	0·340	0·035	0·033	0·011	0·468	0·258	0·259	0·641	0·439
Th	0·0039	0·015	0·0030	0·00062	0·0007	0·0057	0·0058	0·0043	0·061	0·0071
U	0·0028	0·0025	0·0017	0·00040	0·0002	0·0012	0·0035	0·0018	0·054	0·0031

Each column represents an individual spot analysis. All orthopyroxene analyses are next to garnet.

mantle-normalized REE patterns of clinopyroxenes in 1026 V, BC-77, 08BC03, and 08BC08 are shown in Fig 10b. Overall, clinopyroxenes are depleted in HREE relative to LREE, most probably as a result of subsolidus equilibration with garnet. However, HREE concentrations in clinopyroxenes can be highly variable. For example, HREE contents in 1026 V vary by more than a factor of three, the higher values representing the pyroxene cores that have not yet equilibrated with garnet.

Garnet

Garnets in the Sierran peridotites are pyrope-rich (average end-member composition $Py_{65·5}Al_{20·5}Gr_{8·3}$). Major element and trace element compositions of garnets are reported

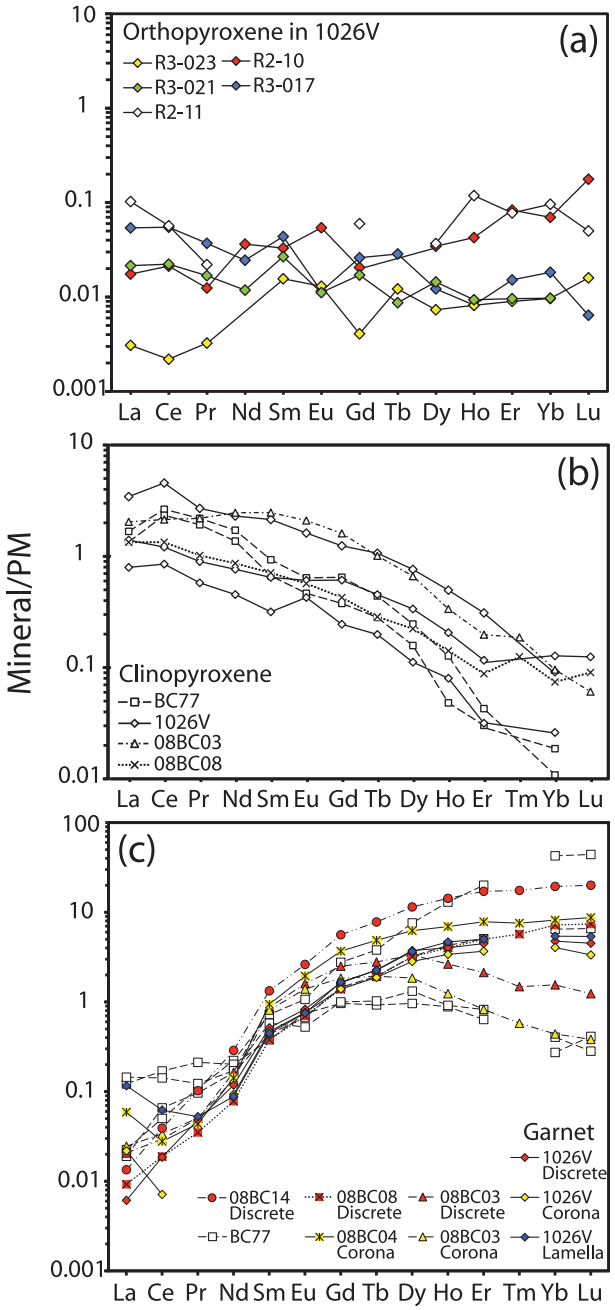

Fig. 10. REE patterns of (a) orthopyroxene in 1026 V, (b) clinopyroxenes in several samples, and (c) garnet in several samples; normalized to primitive mantle (PM).

in Tables 7 and 8. Energy-dispersive (EDS) scans and quantitative WDS spot analyses of cores and rims of garnet indicate the absence of compositional zoning. Interestingly, even though the garnets in the peridotites occur in texturally distinct environments (e.g. lamellae, coronae, and discrete crystals dispersed throughout the matrix), their major element compositions are homogeneous. REE patterns (normalized to primitive mantle) of garnets in samples 1026 V, BC-77, 08BC03, 08BC04, 08BC08, and 08BC14 are shown in Fig. 10c. In general, the garnet REE patterns show positive slopes from La to Lu, although garnets within single samples show a range in enrichment, particularly in MREE and HREE.

Spinel

Major element compositions of spinels are reported in Table 9. As mentioned above, large relict spinels in garnet-bearing spinel peridotites are zoned from low Cr-number [atomic Cr/(Cr + Al) × 100] cores (30–40) to high Cr-number rims (≥50) at the contact with garnet coronas (Fig. 12). The high Cr-number rims near garnet are attributed to the formation of garnet because Cr is more compatible in spinel and will be enriched in a residual spinel as garnet forms. Spinels in spinel peridotites are homogeneous. Interestingly, the cores of large relict spinels in both spinel and garnet-peridotite types record similar Cr-number between 30 and 40. Two garnet-bearing peridotites, 08BC04 and P-1, and one spinel peridotite, P-7, have low Cr-number spinel cores (~10). The green spinels, which probably represent late-stage garnet breakdown products, all have Cr-number in spinel much lower than 10.

Olivine

Olivines are homogeneous within single peridotite samples. Major element compositions are reported in Table 10. The Mg-numbers range from 87·9 to a maximum of 91·5, with the average at 90·5. Ni contents do not vary significantly with Mg-number; Ni contents fall within the range 0·36–0·46 wt %.

GEOTHERMOBAROMETRY

Approach

In this section, we use subsolidus mineral geothermobarometry to constrain the final leg of the *P–T* path with particular emphasis on constraining final equilibration conditions. In the next section, we attempt to extract prior *P–T* conditions (the first leg) by linking the degree of melt depletion, as inferred from whole-rock compositions and relict spinel compositions, to paleo-depths. Because of textural and compositional evidence for disequilibrium (e.g. porphyroclastic texture, major element zonation in minerals, variability in REE content in different mineral grains within the same sample), we intentionally focused on mineral rims, which provide the best opportunity for recording local equilibrium at the final *P–T* at which the system closed. In particular, we examine mineral rim pairs, that is, where two minerals and their rims share a common grain boundary. We used high spatial resolution field-emission electron microprobe imaging

Table 6: Clinopyroxene major element compositions

	Spinel peridotites										
	08BC01		08BC06		08BC-13		P-7		P-10		BC98-2
	Rim	Core	Rim	Core	Rim	Core	Rim	Core	Rim	Core	Core
SiO_2	53·61	53·11	53·57	52·88	53·63	53·35	52·33	52·00	52·73	53·62	54·25
TiO_2	0·21	0·38	0·10	0·11	0·03	0·05	0·40	0·41	0·24	0·21	0·03
Al_2O_3	2·92	4·74	2·79	3·42	1·65	2·39	5·18	4·84	2·61	2·56	1·39
Cr_2O_3	1·30	1·43	0·71	1·06	0·56	0·76	0·83	0·94	0·96	1·02	0·60
FeO	1·57	1·50	1·89	1·76	1·57	1·79	2·31	2·02	1·90	1·79	1·65
MnO	0·05	0·06	0·08	0·06	0·08	0·08	0·09	0·09	0·09	0·07	0·05
MgO	16·76	15·50	17·06	16·76	17·64	17·28	15·92	15·63	16·58	16·67	17·94
CaO	22·95	21·74	24·13	23·69	24·64	24·34	20·87	21·90	23·14	23·01	22·61
Na_2O	1·10	1·79	0·69	0·83	0·38	0·50	1·51	1·28	0·70	0·73	0·76
K_2O	0·01	0·00	0·00	0·00	0·00	0·01					
Total	100·48	100·26	101·01	100·58	100·17	100·54	99·44	99·11	98·95	99·68	99·28
Mg-no.	95·01	94·84	94·15	94·43	95·25	94·51	92·47	93·24	93·96	94·32	95·09

	Garnet-bearing spinel peridotites											
	1026 V		BC77		08BC-03		08BC-04		08BC-08		08BC-14	
	Rim	Core	Rim	Core	Rim	Core	Rim	Core	Rim	Core	Rim	Core
SiO_2	54·54	54·37	54·39	54·33	54·78	54·07	53·24	52·80	54·61	54·10	53·40	53·36
TiO_2	0·03	0·03	0·07	0·08	0·11	0·21	0·58	0·70	0·03	0·06	0·20	0·21
Al_2O_3	1·40	1·62	1·72	1·99	1·77	3·08	4·88	6·36	1·58	2·00	2·71	2·90
Cr_2O_3	0·97	0·90	0·88	0·96	0·74	1·08	0·60	0·68	0·81	0·92	1·14	1·00
FeO	1·85	1·81	2·08	2·11	1·74	1·77	2·45	2·29	1·94	2·10	1·78	1·66
MnO	0·03	0·01	0·05	0·04	0·04	0·01	0·03	0·04	0·06	0·05	0·06	0·03
MgO	17·08	16·99	16·93	17·00	17·12	17·03	15·64	14·35	17·25	17·17	16·72	16·55
CaO	22·72	22·54	22·49	22·27	23·09	21·84	20·78	20·51	23·13	22·66	22·60	22·66
Na_2O	0·94	0·97	1·04	1·10	1·06	1·25	2·04	2·49	0·94	1·05	1·32	1·30
K_2O	0·01	0·01	0·00	0·01	0·00	0·03	0·00	0·00	0·00	0·01	0·00	0·00
Total	99·56	99·25	99·66	99·87	100·44	100·37	100·24	100·23	100·36	100·11	99·94	99·67
Mg-no.	94·28	94·37	93·56	93·50	94·62	94·48	91·92	91·78	94·05	93·57	94·37	94·69

Rims and cores reported below are of the same mineral grain; each column represents a single spot analysis.

to select appropriate rim areas for quantitative analyses. Regions affected by late-stage magmatic infiltration from the host magma or post-eruption alteration were avoided. We calculated final P–T values for five garnet-bearing spinel peridotites: 1026 V, BC-77, 08BC03, 08BC04, 08BC08 (Fig. 13). Owing to extensive serpentinization, samples 08BC14 and 08BC07 did not preserve suitable mineral pairs for geothermobarometry. The textural richness of 1026 V and BC-77 make these two samples especially ideal for detailed geothermobarometry involving garnet lamellae and host orthopyroxene.

Of the variety of textures within the Sierran peridotites, we consider garnet lamellae in large, porphyroclastic orthopyroxenes as providing the best opportunity for unequivocal identification of garnet and orthopyroxene sharing a common grain boundary. Subsolidus equilibration of garnet and orthopyroxene obeys the following net-transfer reaction: $MgAl_2SiO_6 + Mg_2Si_2O_6 = Mg_3Al_2Si_3O_{12}$.

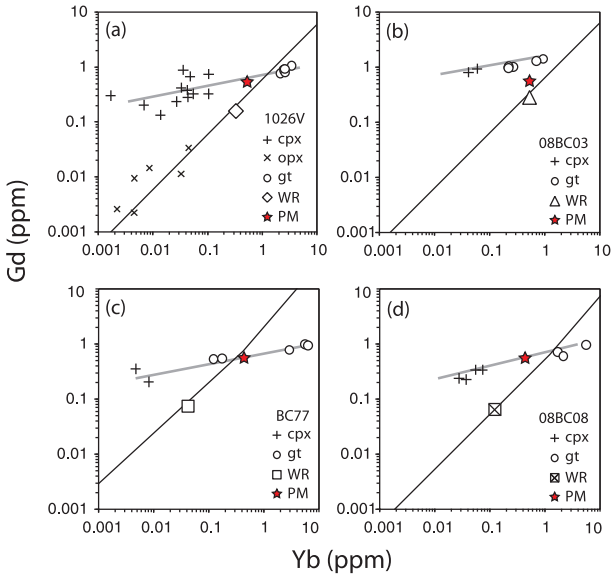

Fig. 11. Variation of Gd vs Yb in clinopyroxene, garnet and orthopyroxene of four Sierran peridotites. Diagonal black lines pass through the whole-rock composition and a point nearly at zero (the coordinates of the whole-rock composition divided by 10 000; this was done to simulate a line forced through zero on a log–log plot). These lines also pass through the region of greatest overlap between garnet and pyroxene analyses. In theory, the lines represent the initial equilibrated whole-rock and garnet-free pyroxene. As garnet exsolves from pyroxene, the initial pyroxene evolves away from the black line along one of the grey lines connecting pyroxenes and garnets within single samples. Although it would be more appropriate to show a straight black line passing through the origin for each sample's population of clinopyroxenes and garnets, only one line is shown here for clarity. (a) 1026 V; (b) 08BC03; (c) BC-77; (d) 08BC08.

Where garnet lamellae are unavailable, we use garnet coronas around relict spinels and discrete garnet–pyroxene pairs. However, geothermobarometric analysis based on discrete mineral grains in texturally and chemically disequilibrated samples is complicated by the difficulty in identifying equilibrated mineral rim pairs because, in many cases, the appropriate minerals do not share a common grain boundary. Use of discrete mineral grains is also complicated by the fact that a multitude of mineral reactions operate. For instance, the transition from spinel to garnet in the upper mantle, manifested texturally by garnet coronas around spinel, is governed by a reaction that involves spinel and orthopyroxene ($MgAl_2O_4 + 2Mg_2Si_2O_6 = Mg_3Al_2Si_3O_{12} + Mg_2SiO_4$) as well as clinopyroxene ($MgAl_2O_4 + 2CaMgSi_2O_6 = Ca_2MgAl_2Si_3O_{12} + Mg_2SiO_4$) (MacGregor, 1964; O'Neill, 1981). Further complications arise from the fact that many of our samples, as we will discuss below, have been refertilized, which can give rise to different generations of pyroxenes or even garnet. For these reasons, garnet lamellae and host orthopyroxene mineral pair geothermobarometry provide the most robust means of 'seeing through' the effects of macro-scale disequilibrium.

Table 7: Garnet major element compositions

	1026 V	BC77	08BC03	08BC04	08BC08	08BC14
SiO_2	42·89	41·24	41·76	41·29	40·87	40·51
TiO_2	0·02	0·04	0·10	0·10	0·02	0·08
Al_2O_3	20·80	22·56	23·18	23·53	22·18	22·88
Cr_2O_3	1·16	1·74	1·46	0·69	2·06	1·52
FeO	9·97	10·23	9·29	10·89	10·16	10·33
MnO	0·49	0·55	0·44	0·52	0·57	0·55
MgO	19·43	18·47	19·18	18·61	18·57	18·65
CaO	4·70	5·20	5·08	4·39	5·51	5·16
NiO	0·08					
Total	99·55	100·02	100·48	100·02	99·94	99·69

Each column represents a single spot analysis. All garnets are unzoned with respect to major elements.

Results: final *P–T* of Sierran peridotites

Spinel peridotites: geothermometry

Owing to the absence of garnet, there are no strongly pressure-dependent reactions in spinel peridotites suitable as robust geobarometers. Recently, some geobarometers for spinel peridotites have been suggested, but these involve the Na content of clinopyroxene in equilibrium with a melt (Putirka, 2008), and therefore are difficult to apply in our study because of significant subsolidus re-equilibration and because the melt composition is not known. Thus, for the spinel peridotites, we focus only on estimating temperatures of equilibration. Using Ca-in-orthopyroxene geothermometry (Brey & Kohler, 1990), Lee *et al.* (2001) showed that cores of orthopyroxene in both Sierran spinel peridotites and garnet-bearing peridotites record temperatures ≥900°C, whereas corresponding orthopyroxene rims record temperatures ≤800°C. Likewise, temperatures of orthopyroxene cores in Sierran garnet-bearing spinel peridotites calculated using the 'Cr–Al–orthopyroxene' geothermometer of Witt-Eickschen & Seck (1991) range from 910 to 1025°C, overlapping the values obtained from Ca-in-orthopyroxene thermometry. These results indicate that spinel peridotites were originally hot, but subsequently cooled to low final temperatures.

Garnet-bearing spinel peridotites

Garnet + orthopyroxene geothermobarometry. The Fe–Mg exchange geothermometer between garnet and orthopyroxene was used in conjunction with a geobarometer based on the solubility of Al in orthopyroxene coexisting with garnet (Harley & Green, 1982; Harley, 1984). We also used the Fe–Mg exchange geothermometer of Harley (1984) with a more recent calibration of the Al-in-orthopyroxene geobarometer of Brey & Kohler (1990), which improves on the older calibration of Harley & Green (1982) by

Table 8: Representative garnet trace element concentrations

	1026V			BC77*						
	Discrete	Corona	Bleb in pyroxene	12-grt	14-grt	18-grt	20-grt	22-grt	46-grt	50-grt
Li	0·318	0·650	10·7	2·86	193	0·108		0·083	0·155	17·3
Ti	236	185	212	244	216	223	241	230	226	221
Co	43·8	42·5	45·9	62·0	51·4	40·8	43·7	43·4	62·9	48·3
Ni	17·3	30·0	15·9	26·0	186	24·0	31·6	15·1	43·9	18·4
Zn										
Rb	0·004	0·069	0·664	0·281	1·76	0·242	0·021	0·151	0·475	0·292
Sr	0·057	0·000	1·84	0·199	21·8	0·422	0·066	0·198	2·84	1·03
Y	17·9	14·7	19·4	44·3	37·1	23·3	28·4	18·2	2·60	3·50
Zr	2·58	2·48	3·04	14·4	13·5	10·1	11·5	10·0	6·05	6·28
Nb	0·335	0·255	0·299	0·323	0·213	0·141	0·145	0·144	0·181	0·115
Cs		0·011	0·496	0·046	1·11	0·018		0·009	0·028	0·082
Ba	0·03	0·49	1·90	5·00	54·6	8·84	0·04	5·55	8·84	7·70
La	0·004	0·014	0·113	0·015	0·030	0·026	0·005	0·012	0·079	0·094
Ce	0·031	0·012	0·104	0·084	0·144	0·153	0·066	0·110	0·285	0·238
Pr	0·012		0·013	0·028	0·034	0·036	0·020	0·025	0·054	0·031
Nd	0·148	0·116	0·110	0·278	0·265	0·311	0·210	0·204	0·252	0·213
Sm	0·209	0·190	0·181	0·295	0·218	0·255	0·185	0·177	0·154	0·235
Eu	0·128	0·117	0·115	0·164	0·152	0·106	0·106	0·103	0·115	0·081
Gd	0·888	0·759	0·906	1·50	1·25	0·978	0·934	0·794	0·524	0·544
Tb	0·225	0·186	0·223	0·376	0·311	0·219	0·248	0·191	0·092	0·102
Dy	2·52	1·91	2·46	5·12	4·34	2·83	2·83	2·18	0·648	0·889
Ho	0·598	0·505	0·695	1·94	1·53	0·891	1·10	0·637	0·132	0·136
Er	1·96	1·61	2·20	8·77	7·21	3·66	4·16	2·22	0·279	0·360
Tm										
Yb	2·10	1·78	2·39	18·8	13·5	5·63	6·44	2·86	0·120	0·178
Lu	0·305	0·226	0·363	2·979	2·401	0·875	1·16	0·445	0·028	0·019
Hf	0·048	0·031	0·065	0·230	0·251	0·178	0·162	0·159	0·110	0·112
Ta	0·002	0·000	0·001							
Pb	0·007	0·058	0·200	0·337	0·951	0·275	0·017	0·188	0·369	0·289
Th	0·001		0·003		0·001	0·001				0·001
U	0·002	0·005	0·003	0·003	0·004	0·004	0·004	0·002	0·003	0·002

	08BC03		08BC04	08BC08	08BC14
	Discrete	Corona	Corona	Discrete	Discrete
Li	1·79	2·37	1·58	3·76	1·93
Ti	689	526	631	204	712
Co	52·1	43·9	45·6	44·8	43·8
Ni	17·8	17·9	99·4	15·8	34·3
Zn	9·38	29·3	64·1	10·7	7·94
Rb	0·197	0·074	0·351	0·110	0·104
Sr	0·234	0·846	0·565	0·330	0·138
Y	10·1	4·60	30·1	16·9	59·7
Zr	11·9	9·52	18·3	2·16	27·8
Nb	0·028	0·059	0·032	0·031	0·083
Cs	0·149	0·023	0·063	0·066	0·047
Ba	0·42	1·89	1·09	0·23	0·41
La	0·013	0·016	0·038	0·006	0·007
Ce	0·050	0·057	0·047	0·032	0·066
Pr	0·013	0·013	0·011	0·009	0·025
Nd	0·205	0·171	0·177	0·098	0·348
Sm	0·353	0·329	0·383	0·154	0·544
Eu	0·247	0·215	0·300	0·107	0·395
Gd	1·36	1·00	2·00	0·754	2·93
Tb	0·276	0·191	0·482	0·189	0·751
Dy	2·25	1·25	4·20	2·15	7·39
Ho	0·394	0·184	1·03	0·598	2·02
Er	0·933	0·362	3·44	2·19	7·23
Tm	0·101	0·039	0·514	0·388	1·15
Yb	0·684	0·194	3·61	3·18	8·30
Lu	0·083	0·026	0·589	0·500	1·31
Hf	0·232	0·178	0·234	0·067	0·424
Ta	0·019	0·009	0·011	0·009	0·009
Pb	0·052	0·024	0·108	0·014	0·006
Th	0·011	0·012	0·035	0·008	0·008
U	0·008	0·012	0·018	0·004	0·006

All analyses are individual spots
*Rims

Table 9: Spinel major element compositions

	Spinel peridotites						
	08BC01	08BC13		P-7		P-10	BC98-2
	Core	Core	Rim	Core	Rim	Core	Core
TiO_2	0·14	0·03	0·03	0·06	0·08	0·22	0·17
Al_2O_3	41·53	35·06	36·88	51·95	51·46	36·64	19·47
Cr_2O_3	27·46	30·30	29·13	14·87	15·25	27·94	49·23
FeO	11·17	16·29	15·24	13·18	12·99	16·65	11·01
Fe_2O_3	1·94	4·68	4·65	2·36	2·43	5·11	4·09
MnO	0·15	0·28	0·20	0·14	0·13	0·25	0·25
MgO	17·87	13·68	14·72	17·66	17·72	13·92	15·64
V_2O_3	0·14	0·18	0·18	0·08	0·09	0·20	0·29
NiO	0·16	0·15	0·18	0·28	0·29	0·18	0·21
ZnO	0·20	0·24	0·30	0·11	0·09	0·12	0·03
Total	100·76	100·90	101·50	100·69	100·53	101·20	100·39
Cr#	30·73	36·70	34·63	16·11	16·58	33·84	62·92
Mg#	74·04	59·96	63·25	70·49	70·86	59·84	71·70

	Garnet-bearing spinel peridotites												
	1026V		BC77	P-1*	P-6	08BC03		08BC04		08BC08		08BC14	
	Core	Rim	Core		Core	Core	Rim	Core	Rim	Core	Rim	Core	Rim
TiO_2	0·15	0·36	0·22	0·09	0·25	0·22	0·49	0·06	0·08	0·17	0·24	0·27	0·56
Al_2O_3	36·97	23·13	34·91	52·40	36·47	41·95	24·94	55·42	53·02	35·77	24·13	41·57	25·89
Cr_2O_3	28·55	41·03	28·41	12·00	28·03	25·13	40·98	11·49	13·80	28·95	39·29	25·25	39·97
FeO	14·97	17·91	16·53	14·60	16·02	12·45	15·34	11·14	12·27	14·50	16·52	12·39	15·18
Fe_2O_3	4·38	6·37	5·37	4·24	4·96	2·62	3·85	2·28	2·64	4·98	6·74	3·24	4·60
MnO	0·22	0·63	0·17	0·18	0·38	0·43	0·58	0·10	0·17	0·51	0·70	0·21	0·34
MgO	14·80	11·59	13·54	16·78	14·15	16·91	13·25	19·24	18·32	14·82	12·24	17·04	13·68
V_2O_3	0·24	0·23	0·33			0·22	0·30	0·11	0·10	0·22	0·38	0·22	0·34
NiO	0·24	0·16	0·24		0·13	0·23	0·16	0·41	0·44	0·21	0·16	0·21	0·15
ZnO	0·36	0·35	0·16		0·09	0·37	0·19	0·20	0·25	0·37	0·31	0·29	0·21
Total	100·87	101·75	99·88	100·29	100·49	100·53	100·07	100·45	101·09	100·52	100·72	100·69	100·94
Cr#	34·12	54·33	35·31	13·32	34·02	28·66	52·43	12·21	14·87	35·19	52·21	28·95	50·87
Mg#	63·80	53·55	59·35	67·20	61·15	70·76	60·62	75·49	72·68	64·57	56·90	71·04	61·63

Cr# = (atomic Cr/(Cr + Al) × 100)
Mg# = (atomic Mg/(Mg + Fe^{2+}) × 100)
Fe_2O_3 was calculated by stoichiometry using the built-in software provided with the Cameca SX 50 electron microprobe at Texas A&M University
*From Dodge et al. (1988)

incorporating the activities of additional elements (Ti, Na, Cr) in orthopyroxene and garnet. We found that the combination of Harley & Green (1982) and Brey & Kohler (1990) resulted in an average maximum temperature difference of 10°C [pressures converged to the same values as obtained using Harley & Green (1982) and Harley (1984)]. Final P–T values plotted in Fig. 13 are those using Harley & Green (1982) and Harley (1984).

For all P–T determinations, we solved the two geothermobarometers for the same mineral pair. This approach is

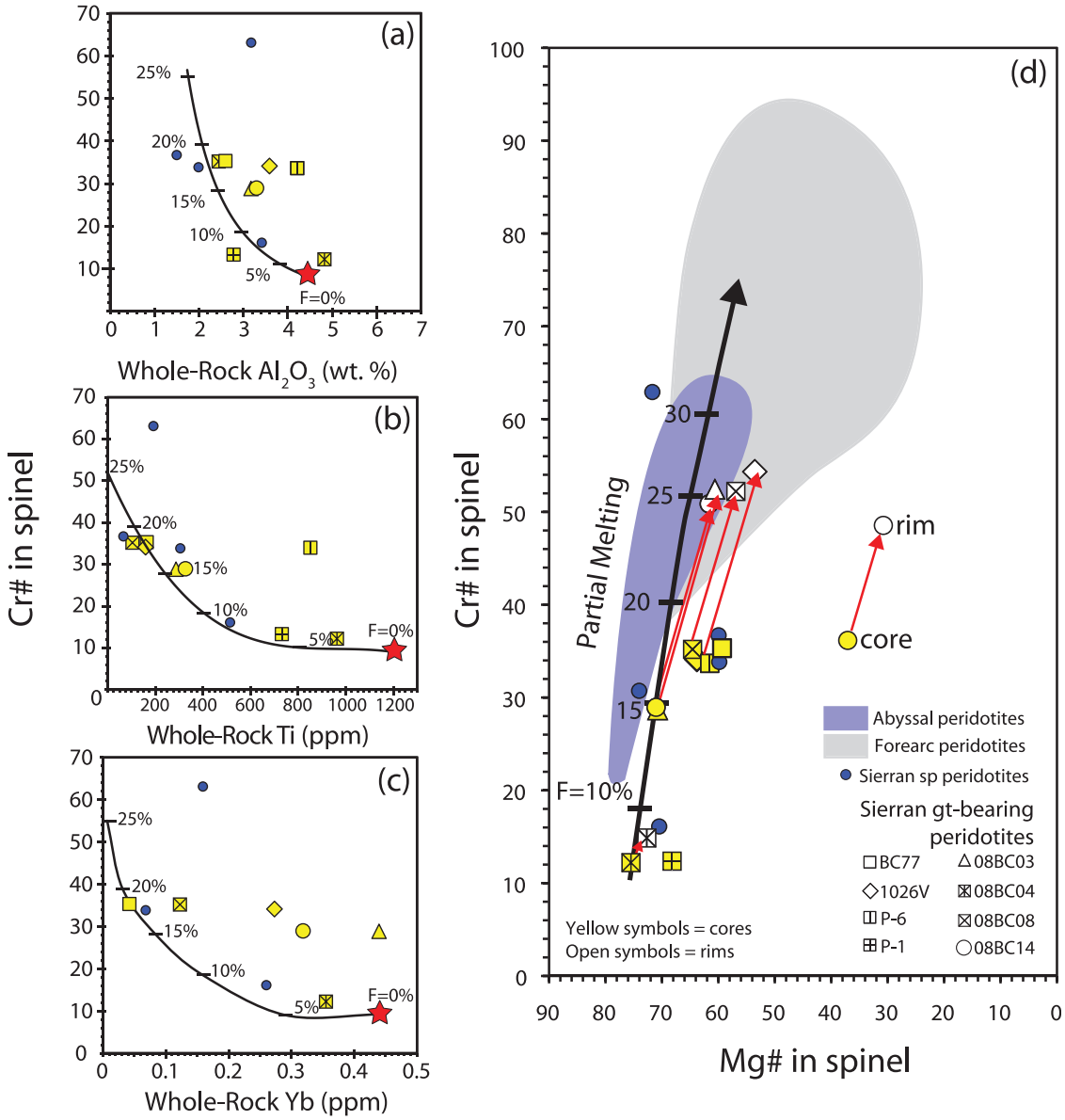

Fig. 12. Geochemistry of chromian spinels in Sierran peridotites (see Fig. 7 for symbols). (a)–(c) show Cr-number [atomic Cr/(Cr + Al) × 100] in spinel vs whole-rock major and trace element contents. Only core compositions of the largest relict spinels are plotted. Continuous black lines are hypothetical melting trends starting from primitive mantle compositions. (a) Cr-number in spinel vs whole-rock Al_2O_3. (b) Cr-number in spinel vs whole-rock Ti. (c) Cr-number in spinel vs whole-rock Yb. (d) Cr-number vs Mg-number [atomic Mg/(Mg + Fe^{2+}) × 100] in spinel for spinel peridotites (small circles) and garnet-bearing spinel peridotites (arrows connect cores to rims of single spinel grains). Overall, spinel cores in both peridotite types (spinel and garnet-bearing) record melt depletion between 15 and 20%. Partial melting trend is after Dick & Bullen (1984), incorporating data from Hirose & Kawamoto (1995) and Matsukage & Kubo (2003). Shaded fields represent global forearc peridotites and abyssal peridotites [data from Arai & Ishimaru (2008)].

preferred over thermobarometric combinations that involve different mineral pairs because errors associated with identifying equilibrated mineral pairs increase if the number of different discrete phases not in local equilibrium increases. Average final equilibration temperatures of the garnet-bearing spinel peridotites are 755°C (670–850°C) and average pressures are 2·8 GPa (2·4–3·6 GPa). Two peridotites, 1026 V and 08BC04, recorded contrasting final *P–T* values using different garnet–orthopyroxene pairs in the same sample (Table 11). For instance, in 1026 V, garnet lamellae + orthopyroxene pairs measured within the pyroxene- and garnet-rich band (see Fig. 4 and inset of Fig. 5) yield pressures of 1·7–2·1 GPa and temperatures of 670–734°C. However, within the large relict orthopyroxene porphyroclast in the same sample, *P–T* values from garnet lamellae + orthopyroxene pairs were in the range

Table 10: Olivine major element compositions

	Garnet-bearing spinel peridotites					
	1026 V	BC77	08BC03	08BC04	08BC08	08BC14
SiO_2	40·55	40·92	40·80	40·80	40·50	40·75
Al_2O_3	0·01	0·01	0·01	0·01	0·00	0·00
FeO	8·90	8·80	8·45	9·67	8·80	8·21
MnO	0·10	0·09	0·11	0·08	0·09	0·08
MgO	49·67	50·14	50·56	49·90	50·02	50·55
CaO	0·00	0·00	0·01	0·00	0·01	0·01
Na_2O		0·03	0·01	0·00	0·00	0·02
NiO	0·36	0·42	0·46	0·42	0·39	0·46
Total	99·59	100·42	100·40	100·87	99·82	100·09
Mg-no.	90·87	91·04	91·43	90·19	91·02	91·65
	Spinel peridotites					
	08BC01	08BC06	08BC13	P-7	P-10	BC98-2
SiO_2	41·40	40·67	40·58	40·20	40·31	40·70
Al_2O_3	0·01	0·00	0·01	0·01	0·01	0·02
FeO	7·18	9·06	8·52	9·90	9·11	8·76
MnO	0·10	0·11	0·12	0·11	0·16	0·15
MgO	51·74	50·07	50·67	49·30	49·41	49·84
CaO	0·01	0·01	0·00	0·01	0·02	0·02
Na_2O	0·00	0·00	0·02			
NiO	0·33	0·39	0·42	0·37	0·38	0·48
Total	100·78	100·31	100·34	99·90	99·40	99·97
Mg-no.	92·78	90·79	91·38	89·88	90·63	91·03

All analyses are single spots.

of 2·9–3·6 GPa and 774–845°C. An important distinction between the two garnet-bearing orthopyroxene grains is that the host orthopyroxene giving the lower apparent P has >1 wt % Al_2O_3, whereas that recording higher apparent P has <1 wt % Al_2O_3.

This inconsistency between final P–T values calculated within different areas of the same sample can be explained by the different closure rates of the Al-in-opx geobarometer and Fe–Mg exchange geothermometer. This is because the diffusion rates of the trivalent cation Al and divalent cations Ca, Mg and Fe in pyroxenes are fundamentally different. For example, at 1000°C, Al diffusivity in pyroxene is $<10^{-22}\,m^2\,s^{-1}$ (Sautter & Fabriès, 1990), but Fe and Mg diffusivities are $\sim10^{-18}$–$10^{-19}\,m^2\,s^{-1}$ (Brady, 1995). These large differences in diffusivity result in very different kinetics of re-equilibration. Thus, the Al distribution between minerals will re-equilibrate more sluggishly than Fe–Mg exchange. In addition, during cooling, Al will 'freeze' in earlier (e.g. at higher temperature) than Fe–Mg exchange, which continues to re-equilibrate to lower temperatures. Thus, Al contents in pyroxenes will more probably record a range of 'arrested' states, whereas Fe–Mg distribution between minerals will converge on a common (and lower) closure temperature. We attribute the differences in orthopyroxene Al_2O_3 content within the same sample, as discussed above, to this phenomenon.

Owing to the different kinetics of the various geothermometers and geobarometers employed, artifacts in estimated P–T are generated. This can be seen in Fig. 14, where we plot calculated P–T values for 1026 V and selected isopleths of constant Fe/Mg distribution between garnet and orthopyroxene (Harley, 1984) and of constant Al in orthopyroxene coexisting with garnet (Harley & Green, 1982). Also plotted in Fig. 14 are the P–T results obtained by previous workers on similar xenoliths from Big Creek (Dodge *et al.*, 1988; Mukhopadhyay & Manton, 1994; Ducea & Saleeby, 1996). Calculated temperatures from these studies are considerably higher than our results; this may be due to those workers using mineral cores instead of mineral rims. We verified this by calculating a few core–core P–T values, and the results were significantly higher than rim–rim P–T values. Nevertheless, all P–T estimates collapse onto a small temperature interval, defining a steep dP/dT array. This indicates that most samples had sufficient time to re-equilibrate their rims to ambient temperatures in the Sierran lithosphere. However, a wide scatter is observed for apparent equilibration P, indicating that the Al-in-opx barometer closed over different P and T conditions, which we attribute to the considerably more sluggish kinetics of Al compared with Fe and Mg. Thus, the lower pressures (and higher Al_2O_3 contents of host orthopyroxene) are most probably artifacts of the Al-in-opx barometer failing to close at the same final state (low Al_2O_3). Interestingly, the large opx porphyroclast in 1026 V, which records the greatest P (3·6 GPa), contains the thickest garnet lamellae as well as the strongest Al-depleted haloes in the pyroxene surrounding the garnet (see traverse in Fig. 5). These two observations suggest a long time interval over which garnet–opx equilibration operated. In contrast, those samples with thin garnet lamellae and thin Al-depleted haloes in surrounding opx suggest shorter time intervals for diffusional exchange, perhaps as a result of different timing of garnet nucleation. In summary, the foregoing analysis indicates that the calculated P values are lower bounds for the actual equilibrium P. Calculated T values may represent the ambient temperature of the deep lithosphere, but given evidence for 'temperature' zonation in pyroxenes as determined from the Ca-in-opx geothermometer (Lee *et al.*, 2001), it is possible that the estimated T values are maximum bounds.

Garnet + 2 pyroxene geothermobarometry. In addition to garnet + orthopyroxene geothermobarometry, we applied

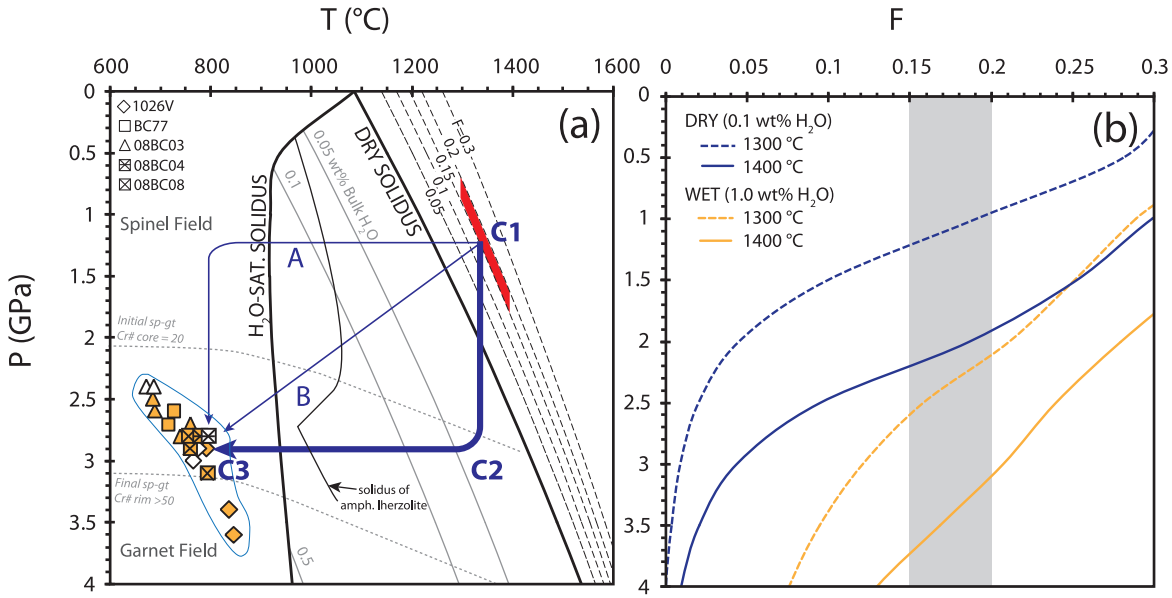

Fig. 13. (a) *P–T* diagram showing final pressures and temperatures of equilibration of the Sierran garnet-bearing spinel peridotites (see Table 11; points that reflect artifacts of the Al-in-opx barometer are omitted). Filled symbols are final *P–T* values calculated using garnet–orthopyroxene geothermobarometry (Harley & Green, 1982; Harley, 1984); open symbols are final *P–T* values calculated using two-pyroxene + garnet geothermobarometry (Ellis & Green, 1979; Krogh, 1988; Brey & Kohler, 1990). Thin dashed curves represent the spinel–garnet transition estimated from the range of Cr-number in Sierran relict spinels (O'Neill, 1981). The low Cr-numbers (0·2–0·4) are of spinel cores and indicate an originally shallow spinel–garnet transition at ~2 GPa. This transition gradually deepens as manifested by the increase in Cr-number from cores to rims, with highest Cr-number (0·6) at the contact with garnet coronas. Also shown on this diagram are contours of *F* (thick dashed black lines), the anhydrous and water-saturated solidus (continuous black lines), and the solidus for various water contents (continuous grey lines); all calculated using the parameterization of (Katz *et al.*, 2003). The range of *F* estimated from Cr-number in spinel of the Sierran peridotites (15–20%) is shown as a shaded parallelogram assuming that the mantle melted by adiabatic decompression at a mantle potential temperature between 1300 and 1400°C. Also shown is the solidus of amphibole lherzolite constrained by Green *et al.* (2010). Three potential *P–T* trajectories (A, B, C) are outlined by arrows (see text for discussion). (b) Isothermal curves showing the relationship between *F* and pressure for 0·1 wt % bulk H_2O (blue) and 1·0 wt % bulk H_2O (red), calculated using Katz *et al.* (2003).

two calibrations of the garnet–clinopyroxene Fe–Mg exchange geothermometer (Ellis & Green, 1979; Krogh, 1988) with the solubility of Al-in-orthopyroxene geobarometer (Brey & Kohler, 1990). We also used the two-pyroxene geothermometer of Brey & Kohler (1990) combined with their geobarometer. However, owing to the secondary, metasomatic origin of clinopyroxene in some of the more depleted peridotites, as well as the scarcity of suitable garnet, clinopyroxene, and orthopyroxene grains adjacent to each other, we have fewer estimates from garnet + two pyroxene geothermobarometry than garnet + orthopyroxene geothermobarometry.

The discrepancy in final *P–T* estimates observed in different areas of the same sample was also seen in results from garnet + two pyroxene geothermobarometry, particularly in peridotite 1026 V. This observation lends further support to the notion of variable closure of the Al-in-opx barometer. For the remaining peridotites, results from garnet + two-pyroxene geothermobarometry were consistent with results obtained from garnet + opx geothermobarometry.

Trace element thermometry. An attempt was also made to calculate final equilibration temperatures using the subsolidus equilibrium distribution of trace elements between clinopyroxene and orthopyroxene (Witt-Eickschen & O'Neill, 2005) using *in situ* laser ablation ICPMS data. Only the MREE (e.g. Ho, Er) and Y yield temperatures that fall within the range calculated from major element data, although the range obtained is large (600–1100°C). The observed distribution of HREE (e.g. Yb and Lu) between cpx and opx (cpx/opx) is extremely low (<3), yielding unreasonably high calculated temperatures (>2000°C). One possible explanation for this unreasonable result is that the calibration of Witt-Eickschen & O'Neill was designed for spinel-facies peridotites rather than garnet peridotites. However, the more likely explanation is that the laser spot size was too large (>30 μm) to obtain the fine spatial resolution necessary for quantifying rim–rim compositions in highly zoned minerals. Like Al, the REE have very low diffusivities and therefore the large spot size of laser ablation prohibits clean analysis of fine-scale rims for proper trace element geothermobarometry.

We also applied the Ni-in-garnet geothermometer (Canil, 1999). This geothermometer assumes that the Ni activity in a peridotitic system is approximately buffered by

Table 11: Thermobarometry of Sierran peridotites

Sample	Equilibria	*T* (°C)	*P* (GPa)	Remarks
08BC04	Gt + Opx*	780	2·8	Corona garnet
		699	*1·2*	*Corona garnet, opx severely fractured*
		695	*1·8*	
		704	*0·9*	*Discrete garnet, heavily kelyphitized; opx severely fractured*
	Gt + 2 Px*	796	2·8	Corona garnet
08BC03	Gt + Opx*	690	2·6	Corona garnet
		685	2·5	Corona garnet
		760	2·7	Discrete garnet
		739	2·8	Corona garnet
	Gt + 2 Px†	672	2·4	Corona garnet
	Gt + 2 Px‡	687	2·4	Corona garnet
08BC08	Gt + Opx*	760	2·9	Discrete garnet
		757	2·8	Corona garnet
		794	3·1	Discrete garnet
BC77	Gt + Opx*	718	2·7	Garnet lamellae in large, bent opx porphyroclast
		728	2·6	
1026 V	Gt + Opx*	836	3·4	Garnet lamella in large, bent opx porphyroclast; hosted within recrystallized olivine-dominated matrix
		845	3·6	
		792	2·9	
		706	*1·9*	*Garnet lamella in small opx in diffuse pyroxene-rich band*
		734	*2·1*	
	Gt + 2 Px†	766	3	Both Opx and Cpx contain garnet lamellae
	Gt + 2 Px‡	774	2·9	
	Gt + Ol§	*787*	*2·2*	*Garnet lamella + olivine inclusion in Opx; hosted within diffuse pyroxene-rich band*
	Gt + 2 Px†	*781*	*2·2*	*Within diffuse pyroxene-rich band*
	Gt + 2 Px¶	*720*	*2*	
	Gt + 2 Px‡	651	2·3	

Results in italics represent artefacts of the Al-in-opx barometer and are not shown in final *P–T* diagram.
*Harley & Green (1982); Harley (1984).
†Brey & Kohler (1990).
‡Krogh (1988); Brey & Kohler (1990).
§O'Neill & Wood (1979); Brey & Kohler (1990).
¶Ellis & Green (1979); Harley & Green (1982).

the olivine Ni content (Griffin *et al.*, 1989). We applied this geothermometer only to discrete garnets within the olivine matrix (garnet lamellae were avoided). Temperatures obtained from this geothermometer range between 839 and 928°C, higher than those obtained from Fe–Mg exchange thermometry between garnet and pyroxene.

Spinel–garnet transition constraints on P. We have also constrained final pressures using the Cr-number of relict spinel, which is a sensitive indicator of the pressure at which the spinel–garnet transition occurs in the upper mantle (O'Neill, 1981; Klemme, 2004). Relict spinels in the garnet-bearing spinel peridotites have low Cr-number cores (20–30), corresponding to a spinel–garnet transition of 2·2 GPa at 900°C, and thus indicate that these relict spinels formed at pressures less than ~2·2 GPa. In contrast, rims of spinels in contact with garnet coronas have high Cr-number (≥50), corresponding to a deeper spinel–garnet transition at ~3 GPa at 900°C (O'Neill, 1981). The observation that spinels in the spinel peridotites are unzoned and record similar Cr-numbers to the cores in relict spinels in the garnet-bearing peridotites is strong evidence that the spinel peridotites are the shallower protoliths of the garnet-bearing spinel peridotites, which we discuss in detail below.

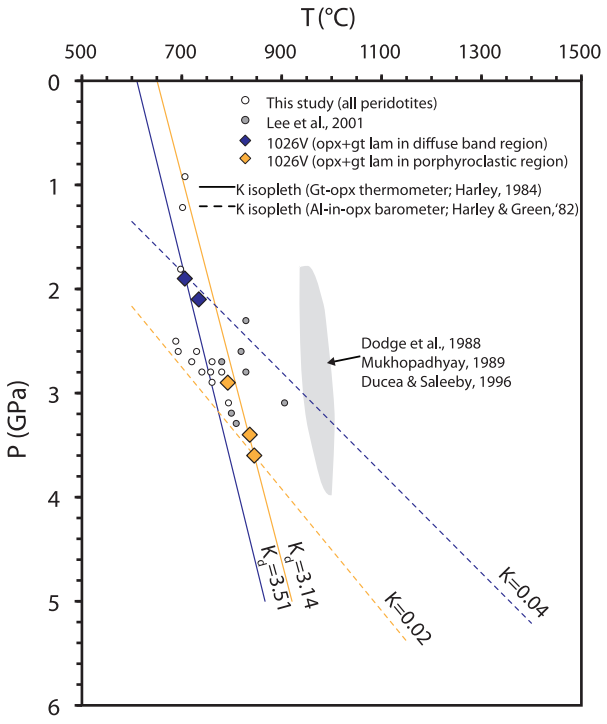

Fig. 14. P–T diagram illustrating how artifacts in calculated P–T are generated owing to the different reaction kinetics of the geothermometers and geobarometers. In this figure, the final P–T calculated using garnet lamellae + orthopyroxene pairs from different areas within one sample, l026 V, record a narrow interval of final temperatures, but a wide array of final pressures. The darker and lighter shaded diamonds represent garnet + opx pairs in two distinct areas of the sample. Dashed lines represent lines of constant K, defined as $(Fe/Mg)_{gt}/(Fe/Mg)_{opx}$ ('iso-K line') for the garnet–orthopyroxene thermometer of Harley (1984) and continuous lines represent lines of constant K_d, defined as $[X_{Al}^{M1}(1-X_{Al}^{M1})/(1-X_{Ca}^{ga})^3]$ for the Al-in-opx barometer of Harley & Green (1982). Also plotted as open circles are all peridotites in this study for which final P–T were calculated, and plotted as filled circles are peridotites from Lee *et al.* (2001). Shaded field represents final P–T range of peridotites from previous studies on Big Creek xenoliths (see Dodge et al., 1988; Mukhopadhyay, 1989; Ducea & Saleeby, 1996).

DEGREE OF MELT DEPLETION OF SIERRAN PERIDOTITES

Cr-number in spinel as an indicator of melt depletion

In this section, we estimate the melting degree (F) of the peridotites. Such information can be used to estimate depths of melt extraction using the relationship between F and P from mantle melting parameterizations (Katz *et al.*, 2003; Langmuir *et al.*, 2006). Methods of estimating F of peridotites involve tracking the depletion or enrichment of an element during partial melting. The Cr-number of spinel has been demonstrated to be sensitive to petrogenetic processes such as fractional crystallization and melting, owing to the high compatibility of Cr in the solid and the incompatibility of Al during peridotite partial melting (Dick & Bullen, 1984). Experimental studies (Hirose & Kawamoto, 1995; Matsukage & Kubo, 2003) verify this by showing a positive correlation between F and spinel Cr-number. A further advantage of using spinel Cr-number is that Cr and Al diffuse slowly, so spinel Cr-number may be more likely to preserve the original signature of a melt depletion even if the rock has been subsequently refertilized.

One caveat in employing Cr-number in spinel as a melt-depletion indicator is that the formation of garnet coronas preferentially extracts Al from the spinel, leaving a 'residual' spinel with an anomalously higher Cr-number (O'Neill, 1981; Webb & Wood, 1986; Obata & Morten, 1987). This is a concern for the Sierran peridotites because the majority of spinels are rimmed by garnet, leading to spinels with Cr-enriched rims owing to equilibration with garnet. Failure to obtain the original Cr-number of spinel before garnet formation can lead to spurious estimates of melting degree. We thus focus on spinel cores because they provide the most meaningful Cr-number signature of melt depletion. Some garnet-mantled spinels are large enough that Cr-enrichment remains confined to a sharply defined rim, as shown by nearly opaque rims and a largely homogeneous, amber-colored interior, suggesting preservation of the original spinel composition in the core. In these coronas, the ratio of garnet to spinel is low, indicating only limited conversion of spinel to garnet. In contrast, coronas in which the garnet to spinel ratio is large are often characterized by small spinels that are either completely opaque or show continuous zonation from rim to core. The effect of garnet corona formation at the expense of spinel on the spinel Cr/Al ratio is modeled in the Electronic Appendix (available for downloading at http://www.petrology.oxfordjournals.org) using exchange reactions and partitioning relationships based on Webb & Wood (1986). The model results show that appreciable changes in spinel Cr-number occur after ~50% of the system has been converted to garnet. Focusing on the core compositions of the largest spinels should thus circumvent the 'garnet formation effect'. With the above considerations in mind, we use Cr-numbers from only the largest relict spinels in both spinel and garnet-bearing peridotites. We find that spinel core Cr-numbers in both peridotite types are consistently between 30 and 40, which corresponds to melting degrees between 0·15 and 0·20 (Fig. 12).

Whole-rock composition as an indicator of melt depletion

We can also estimate F by comparing whole-rock compositions with modeled whole-rock melt-depletion trends. We choose moderately incompatible elements, such as Al, Ti, and Yb, because unlike highly incompatible elements such as the LREE, moderately incompatible elements will not be depleted as rapidly during melting, and thus are useful

as an indicator of melting degree over a wide range of *F*. In addition, moderately incompatible elements are less probably disturbed by cryptic metasomatism compared with highly incompatible elements. We modeled partial melting by starting with a primitive mantle source (McDonough & Sun, 1995) and assuming melting occurred in the spinel stability field, because the protoliths of the garnet-bearing spinel peridotites were garnet-free (see above discussion). We use a non-modal, fractional melting model with mineral modes from Johnson *et al.* (1990). Mineral/melt partition coefficients for Yb (at 1400°C) were taken from Lee *et al.* (2007*a*). Mineral/melt partition coefficients for Ti were those used by Johnson *et al.* (1990). For Al_2O_3, we used the parameterization of Canil (2002), which constrains the bulk-rock/melt partition coefficient of Al_2O_3 as a function of *F*.

The modeled whole-rock Al_2O_3, Ti, and Yb melt-depletion curves are shown in Figs 8 and 12. In Fig. 8, we plot Ti vs Yb and Ti and Yb vs Al_2O_3. In Fig. 12, we show melt-depletion curves involving Cr-number in spinel with Al_2O_3, Ti, and Yb. As expected, melt depletion results in positive correlations between Al_2O_3, Ti, and Yb, and negative correlation between spinel Cr-number and whole-rock Al_2O_3, Ti and Yb. Inspection of these plots reveals that the Sierran peridotites fall on the Cr-number in spinel vs whole-rock Ti melting curves but not on the Cr-number–Yb and Cr-number–Al_2O_3 melting curves. Whole-rock Al_2O_3 and Yb deviate from predicted melting trends to higher values than that expected for a given spinel Cr-number. Al_2O_3 and Yb also appear to be decoupled from melt-depletion trends plotted against Ti as can be seen by excess Al_2O_3 and Yb for a given Ti (Fig. 8). We note that whole-rock Yb and Al_2O_3 are correlated, but because neither Al_2O_3 nor Yb correlate with spinel Cr-number, the correlation between Yb and Al_2O_3 may instead reflect refertilization. In addition, most garnet-bearing spinel peridotites having whole-rock Na_2O contents greater than primitive mantle values also fall off predicted Cr-number in spinel vs Na_2O melt-depletion curves. As with Yb and Al_2O_3, Yb and Na_2O also show a positive correlation, consistent with a refertilization origin for such trends. In contrast, the adherence of whole-rock Ti and Cr-number in spinel to modeled melt-depletion trends suggests that Ti and Cr remained largely unperturbed and thus retain the original melt-depletion signature of the garnet-bearing spinel peridotites. We attribute the preserved record of melt depletion in spinel Cr-number and whole-rock Ti content, in light of a more fertile major element composition for the whole-rock, to reflect disequilibrium. In summary, spinel Cr-number and whole-rock Ti both indicate overall melting degrees of $\geq 15\%$ (relative to a primitive mantle major element composition) for the Sierran peridotites.

DISCUSSION: SYNTHESIS OF *P–T*–COMPOSITION PATH

Summary of textural, geothermobarometric, and geochemical observations

Al contents of orthopyroxene coexisting with garnet and Cr-number in spinel coexisting with garnet indicate that the garnet-bearing spinel peridotites achieved final equilibration at <750°C and pressures ~3 GPa (~90 km). However, textural and chemical evidence indicates that the garnet-bearing spinel peridotites represent metamorphosed melt-depleted spinel peridotites. First, abundant garnet coronas around spinels indicate a transition from spinel to garnet facies. Second, orthopyroxene cores have Al_2O_3 contents too high to be in equilibrium with garnet and instead are similar to the Al_2O_3 contents of orthopyroxene in spinel-facies peridotites [see also Lee *et al.* (2001)]. Third, relict deformed orthopyroxenes contain numerous garnet lamellae accompanied by Al-depletion haloes in the adjacent pyroxene, suggesting garnet exsolved from originally high-Al pyroxene, also typical of spinel-facies peridotites. Fourth, low whole-rock HREE contents point to the absence of garnet during melt depletion. Fifth, spinels in both spinel peridotites and garnet-bearing spinel peridotites share compositional and textural features that demonstrate a common petrogenesis—Cr-number in spinel cores of both peridotite types are identical. This overall conversion of spinel peridotites to garnet-bearing spinel peridotites was accompanied by a progressive decrease in olivine grain size and the development of weak pyroxene foliation bands. We interpret these changes in metamorphic texture to reflect the transformation of a coarse-grained, undeformed spinel peridotite protolith (e.g. 08BCl3 in Fig. 4) into an increasingly recrystallized, slightly deformed spinel peridotite (P-7), and finally into fine-grained, porphyroclastic, deformed garnet-bearing peridotite (1026 V). This transformation of a spinel peridotite protolith to garnet peridotite also appears to have been accompanied by refertilization.

Constraints on the first leg of *P–T* path using melt depletion as a proxy for paleo-depth

The question that now arises is how was the transition from spinel to garnet facies achieved? There are two end-member scenarios. The first is isobaric cooling of a residue that melted at the final equilibration pressure (~3 GPa). The second is shallow melting in the spinel stability field, followed by compression and cooling into the garnet field. The degree of melting (*F*) experienced by upwelling mantle depends on the extent to which such mantle lies above the solidus. Because the solidus has a positive dP/dT, this means that *F* is controlled by *T* and *P*. The higher the temperature and lower the pressure, the higher *F* will be. Our objective is to obtain *P*

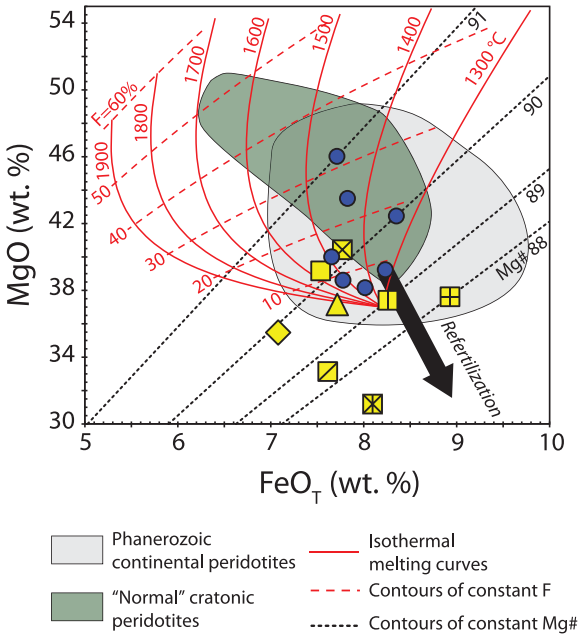

Fig. 15. Plot of whole-rock FeO vs MgO wt % for typical peridotites following the approach described by Hanson & Langmuir (1978) and modified by Lee *et al.* (2011). Dark shaded field represents 'normal' (not silica-enriched) cratonic peridotites and light shaded field represents Phanerozoic continental peridotites for reference. Filled circles represent Sierran spinel peridotites and symbols represent Sierran garnet-bearing spinel peridotites (see Fig. 7 for key to symbols). Continuous lines represent isothermal melting paths, dashed lines represent lines of constant melting degree, and dotted lines represent isopleths of constant whole-rock Mg-number. Arrow schematically points in the direction of refertilization. (See Elecronic Appendix for details and calculations of the various lines shown in the figure.)

corresponding to the original P of the spinel peridotite protoliths of the garnet-bearing peridotites. To do this, we need estimates of F and T. Based on Cr-number in relict spinel cores and whole-rock Ti contents, as discussed above, estimated melting degrees range between 15 and 20%. Temperature of melting can be bounded by assuming reasonable mantle potential temperatures (e.g. 1300–1400°C) but a less arbitrary approach is to use the temperature dependence of Fe and Mg partitioning between olivine and basaltic melt. This approach is shown in Fig. 15 and is based on that of Hanson & Langmuir (1978), as modified by Lee *et al.* (2011). It can be seen that at temperatures <1300°C, Fe becomes compatible such that the FeO content of peridotites increases with melting degree (this approach does not depend on water because the effect of water is to depress the solidus, which in turn changes the compatibility of Fe and Mg because the temperature of melting is decreased). Ignoring those samples that have experienced refertilization (e.g. the samples with low MgO and low Mg-number) it can be seen that the most melt-depleted peridotites (high Mg-number) have low FeO contents and thus are best explained by melting at temperatures between 1300 and 1400°C.

We now input these constraints on F and T into anhydrous and hydrous melting models. To achieve F >15 % at reasonable mantle potential temperatures (1300–1400°C) under anhydrous (<0·1 wt % H_2O) conditions, final pressures of melting of ~1·5 GPa (~45 km) are required (Fig. 13). To achieve the same melting degree at the present equilibration pressures of the garnet peridotites (3 GPa), temperatures >1500°C are needed (Katz *et al.*, 2003), which seems unlikely given the above constraints on original melting temperatures. However, if higher water contents are assumed, this temperature constraint can be relaxed because the effect of hydration is to depress the solidus and increase the melting degree for a given temperature and pressure. We have assessed the effect of hydration using the parameterizations of Katz *et al.* (2003) and assuming the case where bulk H_2O is 1 wt %, a maximum bound on peridotite water content based on inverting the typical water contents of arc basalts (Kelley *et al.*, 2010) for source composition (Fig. 13). At 1300–1400°C, it can be seen that 15–20% melting under water-fluxed conditions can occur at 2·5–3·5 GPa. Because we do not know the original water contents of the unmelted peridotite protoliths, nor do we know the amount of water fluxed through the system during melting, it would seem from these models alone that both high-P and low-P origins are permissible, and thus we are unable to distinguish between the end-member scenarios discussed above.

There are, however, reasons why hydrous fluxed melting at 3 GPa is probably unlikely to explain the petrogenesis of these peridotites. First, pressures of 3 GPa correspond to depths of ~100 km, approaching the typical depth of the slab beneath volcanic arcs (100–110 km). In such proximity to the cold slab, the asthenospheric mantle wedge would be expected to be colder than the ambient mantle. Hydrous flux melting should also initiate melting at temperatures (~900°C) corresponding to the water-saturated peridotite solidus (Katz *et al.*, 2003). Instead, the temperatures inferred from whole-rock FeO and MgO contents (1300–1400°C), as discussed above (Fig. 15), are far higher than the water-saturated solidus, and thus suggest derivation from the hot core of the asthenospheric mantle wedge. Finally, if water-saturated melting had occurred, these peridotites should have been within the stability field of amphibole, which can extend to 3 GPa (Green *et al.*, 2010). Given that these samples are cold and hence well within the amphibole stability field, water-saturated conditions should have been manifested in the presence of primary amphiboles, but this is not seen.

We consider the second end-member, shallow anhydrous melting in the spinel stability field followed by compression to and cooling in the garnet stability field, as our preferred hypothesis. This view is corroborated by the nature of Cr-number zoning in the spinels mantled by garnet coronas. As discussed above, the low Cr-number of the spinel

cores limits the original pressure to be <2·2 GPa, whereas the Cr-number of the spinel rim in contact with garnet coronae suggests final pressures of ~3 GPa. Based on these discussions, we are left with a spectrum of possible P–T paths, all involving an increase in P (Fig. 13a). One extreme path (path A in Fig. 13) is the case of shallow melt depletion, followed by (shallow) isobaric cooling, and then rapid, near-adiabatic compression. At the other extreme is path C wherein the peridotites first experience shallow melt depletion at C1, then undergo adiabatic compression at high temperatures (C2) followed by isobaric cooling at high pressures (C2 to C3). Somewhere between these two extremes is path B, where cooling and compression occur in tandem. In the next section, we attempt to select the most likely of these P–T paths.

Additional constraints from patterns of refertilization

As discussed above, many Sierran garnet-bearing spinel peridotites do not fall on conventional melting trends through canonical primitive mantle (Figs 7 and 8). In addition, some samples show excess whole-rock CaO, manifested in the form of diffuse clinopyroxene bands that define a weak foliation. These features all hint at post melt-depletion refertilization by basaltic melts. The most important feature in the context of this study, however, is that the deepest samples show the largest excesses of whole-rock Yb for a given spinel Cr-number. This excess Yb is correlated mineralogically with the presence of garnet. This implies that Yb was scavenged from the refertilizing melts by pre-existing garnet or that Yb was added to the peridotite because of garnet precipitation from the melt. The overall REE pattern of most of the Sierran garnet-bearing peridotites, with enriched HREE relative to MREE, also suggests that metasomatic garnet was added to a previously melt-depleted spinel peridotite protolith.

In either case, refertilization must have occurred in the garnet stability field, not in the spinel stability field. Thus, refertilization is constrained to occur on the high-pressure leg of the P–T paths described above. We note that the temperatures of the refertilizing melts were most probably above 1000°C, because it seems highly unlikely that refertilization could have occurred at the cold final equilibration temperatures of ~700°C, conditions at which the passage of such melts would have re-requilibrated the cooling-related core-to-rim chemical zonation. If these interpretations are correct, refertilization therefore happened at high P and high T, ruling out P–T path A wherein cooling occurs at shallow pressures followed by an increase in pressure. The most likely P–T path is path C, wherein the peridotites first melt at low P and high T, then experience an increase in P at high T, followed by refertilization at depth and finally by cooling at high P. In a subsequent paper, we will discuss what this refertilizing magma may have been, but further discussion is beyond the scope of the present paper. We only highlight the fact that whole-rock Ti and other HFSE, such as Nb, are depleted relative to the REE. These geochemical signatures are consistent with those of typical subduction zone magmas.

IMPLICATIONS FOR EVOLUTION OF CONTINENTAL ARCS

We have shown that the deep Sierran lithospheric mantle was initially melt-depleted at shallow pressures between 1 and 2 GPa, then experienced compression and cooling, finally reaching equilibration within the garnet stability field at ~3 GPa. Based on additional constraints on the depth at which refertilization occurred, we also conclude that the peridotites increased in pressure at high temperatures, then became refertilized, and finally cooled isobarically at high pressures (path C in Fig. 13).

We now return to the various thickening scenarios described in the Introduction (Fig. 2). Underplating of melt-depleted mantle to the base of pre-existing lithosphere (Fig. 2c) is one mechanism of thickening. However, in such a scenario, a given parcel of underplated material will never experience an increase in P because the overburden weight remains constant (and may even decrease if there is erosion at the Earth's surface). Such mantle would experience isobaric cooling. More likely scenarios for explaining path C are tectonic thickening (Fig. 2a) and magmatic inflation via sill-like intrusions in the crust or mantle lithosphere (Fig. 2d). In the case of tectonic thickening, we can probably rule out thickening resulting from suturing of arc terranes onto the North American margin. These events ended by the Triassic (Dickinson, 1981), but the melt depletion recorded by the peridotite xenoliths was most probably accompanied by significant magmatism, which occurred in the Cretaceous (Lee *et al.*, 2000). Although there is considerable evidence for mega-scale continental underthrusting during the peak of Cretaceous arc magmatism (e.g. Ducea & Barton, 2007; DeCelles *et al.*, 2009) we consider this process an insufficient explanation for the P–T history recorded by the peridotite xenoliths, because such a scenario would result in extensive heating of the underthrusted continental lithosphere, and this is not seen.

We suggest that thickening via magmatic inflation during the main arc-building stage is better able to explain the P–T history of the deep Sierran lithosphere. The Late Cretaceous Sierra Nevada experienced an incredibly high magmatic flux in a short time period: in the span of ~10 Myr, over 4000 km^2 of new crust was emplaced (Coleman & Glazner, 1997). With this context in mind, we envision the following scenario. Shallow, moderate- to high-degree melting within the spinel stability field characterizes the early stages of arcs because the lithosphere is initially

thin, allowing more headspace for decompression melting. As magmas rise into the crust, they reach a depth of neutral buoyancy, generating sills. Progressive addition of these sills results in the thickening of the arc crust by magmatic inflation. Any rocks below the intrusion depth will progressively increase in pressure owing to the gradual increase in overburden pressure generated by magmatic inflation. These processes subsequently compress the deep lithosphere to greater depths. Because this compression is intimately linked with magmatic addition, this model would predict compression at relatively high temperatures, consistent with our interpreted P–T path. We suggest that refertilization occurred after the lithosphere became thickened (3 GPa, equivalent to ~90 km). After thickening and refertilization, the lithosphere cooled to temperatures as low as 700°C. Such low temperatures can be attained only in ambient mantle near a cold subducting slab. We thus suggest that cooling took place after magmatic inflation had increased the thickness of the Sierran lithosphere to depths approaching the subducting slab interface (typically ~100 km beneath arc fronts) (Syracuse & Abers, 2006; Grove *et al.*, 2009; England & Katz, 2010), thereby pinching out the hot asthenospheric mantle wedge and juxtaposing Sierran deep lithosphere against the cold subducting Farallon plate. Thus, the cooling recorded by the peridotites is the result of deep refrigeration by the subducting Farallon plate. Such cooling is predicted to be rapid because of the strong thermal contrast between the slab and mantle lithosphere. Indeed, the presence of Al-depleted haloes next to garnet lamellae (Fig. 5) requires cooling to be fast enough to preserve these features. Testing this hypothesis further will require geochronological constraints on the timing of cooling of the deep lithospheric mantle.

If our proposed P–T and compositional history is correct, there are implications for the magmatic evolution of North American Cordilleran belt. Magmatism in the Sierra Nevada appears to have shut down abruptly around 80 Ma, an observation used as evidence for the onset of 'flat' subduction (Bird, 1988; Lipman, 1992). However, the presence of deep arc lithosphere as recorded by the Sierran xenoliths has been used to argue that 'flat' subduction never occurred beneath the Sierra Nevada (Saleeby, 2003). Could the Sierran continental arc magmatism have terminated simply because it grew too thick to allow for decompression melting and for the presence of the hot asthenospheric mantle wedge necessary to heat and dehydrate the subducting slab?

CONCLUSIONS

We have shown that the deep Sierran lithosphere, represented by a suite of peridotite xenoliths, first experienced hot, shallow melting (1–2 GPa, >1000°C). It was then transported at high temperatures to pressures of ~3 GPa and then subsequently cooled to temperatures below 800°C. This P–T path transformed the spinel peridotites into garnet-bearing spinel peridotites. Refertilization of the arc lithosphere appears to have predominantly affected the deepest equilibrated samples, and, based on the preservation of deformation textures and chemical zonation, occurred before cooling. These observations suggest that refertilization occurred during the compressional stage of the P–T path. Evidence supporting this P–T path is briefly recapitulated below.

(1) Spinel peridotites are characterized by coarse-grained, protogranular, nonfoliated textures. Garnet-bearing spinel peridotites, however, are characterized by fine-grained, recrystallized, porphyroclastic textures. Garnet-bearing peridotites also show a weak foliation defined by diffuse bands of clinopyroxene and/or garnet, suggesting melt infiltration. In addition, garnet-bearing peridotites contain ubiquitous relict spinels rimmed by garnet coronas. Some samples also contain relict orthopyroxene that exsolved garnet lamellae.

(2) Garnet–orthopyroxene geothermobarometry indicates that the garnet-bearing spinel peridotites have final equilibration pressures between 2·4 and 3·6 GPa and temperatures between 670 and 870°C.

(3) Cr-number in relict spinel cores in both spinel peridotites and garnet-bearing spinel peridotites falls between 30 and 40, corresponding to 15–20% melting.

(4) High Al_2O_3 (>4 wt %) in orthopyroxene cores, low whole-rock HREE contents, and the anomalously high mantle potential temperatures (>1500°C) associated with 15 – 20% melting at ~3 GPa preclude deep melting at the pressures of final equilibration, but rather favor melt depletion at shallow pressures (1–2 GPa) within the spinel stability field.

(5) Refertilization has affected almost all the garnet-bearing spinel peridotites, and is manifested by excess whole-rock CaO and Yb, corresponding to excess clinopyroxene and garnet. Spinel peridotites have escaped substantial (i.e. modal) refertilization.

We interpret the Sierran peridotites as representing new lithospheric mantle formed by shallow decompression melting during Cretaceous arc magmatism. This newly generated lithospheric mantle underwent an increase in pressure and a decrease in temperature. We speculate that this P–T path was associated with magmatic inflation that thickened the arc, although tectonic thickening may have also been operating. As the arc thickened, melt-depleted peridotites formed at shallow depths were transported to greater depths where they became more susceptible to refertilization. Thickening continued until the Sierran arc lithosphere impinged against the subducting Farallon plate. This terminated arc magmatism and

resulted in the conductive cooling of the Sierran lithosphere owing to refrigeration by the cold Farallon plate.

ACKNOWLEDGEMENTS

We thank Oliver Jagoutz, Keith Putirka, Maasaki Obata, and Editor Marjorie Wilson for helpful reviews; Jay Ague and Jim Eckert for access to and help on the Yale EPMA; and Ray Guillemette for help on the Texas A&M EPMA. E.J.C. also thanks Steve Nelson for first kindling her enthusiasm for mantle xenoliths as an undergraduate at Tulane University.

FUNDING

This research was initiated with Rice University teaching fellowships to E.J.C. and a Packard Fellowship to C.-T.A.L.; E.J.C. and the project were also supported by NSF EAR 1119315 grant to C.-T.A.L.

SUPPLEMENTARY DATA

Supplementary data for this paper are available at *Journal of Petrology* online.

REFERENCES

Annen, C., Blundy, J. D. & Sparks, R. S. J. (2006). The genesis of intermediate and silicic magmas in deep crustal hot zones. *Journal of Petrology* **47**, 505–539.

Arai, S. & Ishimaru, S. (2008). Insights into petrological characteristics of the lithosphere of mantle wedge beneath arcs through peridotite xenoliths: a review. *Journal of Petrology* **49**, 665–695.

Armstrong, R. (1968). Sevier Orogenic Belt in Nevada and Utah. *Geological Society of America Bulletin* **79**, 429–458.

Arndt, N. T. & Goldstein, S. L. (1989). An open boundary between lower continental crust and mantle: its role in crust formation and crustal recycling. *Tectonophysics* **161**, 201–212.

Atwater, T. (1970). Implications of plate tectonics for the Cenozoic tectonic evolution of western North America. *Geological Society of America Bulletin* **81**, 3513–3536.

Barton, M. D. (1996). Granitic magmatism and metallogeny of southwestern North America. In: Brown, M., Candela, P. A., Peck, D. L., Stephens, R. J. W. & Zen, E.-a. (eds) *The Third Hutton Symposium on the Origin of Granites and Related Rocks. Geological Society of America, Special Papers* **315**, 261–280.

Bird, P. (1988). Formation of the Rocky Mountains, Western United States: a continuum computer model. *Science* **239**, 1501–1507.

Boyd, F. R. & Mertzman, S. A. (1987). Composition and structure of the Kaapvaal lithosphere, Southern Africa. In: Mysen, B. O. (ed.) *Magmatic Processes: Physicochemical Principles. Geochemical Society Special Publication* **1**, 1–13.

Brady, J. B. (1995). Diffusion data for silicate minerals, glasses, and liquids. In: Ahrens, T. J. (ed.) *Mineral Physics and Crystallography: A Handbook of Physical Constants*. Washington, DC: American Geophysical Union, pp. 269–290.

Brey, G. P. & Kohler, T. (1990). Geothermobarometry in four-phase lherzolites II. New thermobarometers, and practical assessment of existing thermobarometers. *Journal of Petrology* **31**, 1353–1378.

Canil, D. (1999). The Ni-in-garnet geothermometer: calibration at natural abundances. *Contributions to Mineralogy and Petrology* **136**, 240–246.

Canil, D. (2002). Vanadium in peridotites, mantle redox and tectonic environments: Archean to present. *Earth and Planetary Science Letters* **195**, 75–90.

Carlson, R. W., Pearson, D. G. & James, D. E. (2005). Physical, chemical, and chronological characteristics of continental mantle. *Reviews of Geophysics* **43**, RG1001.

Chen, J. H. & Moore, J. G. (1982). Uranium–lead isotopic ages from the Sierra Nevada Batholith, California. *Journal of Geophysical Research* **87**, 4761–4784.

Coleman, D. S. & Glazner, A. F. (1997). The Sierra Crest magmatic event: rapid formation of juvenile crust during the Late Cretaceous in California. *International Geology Review* **39**, 768 – 787.

Coney, P. J. & Harms, T. A. (1984). Cordilleran metamorphic core complexes: Cenozoic extensional relics of Mesozoic compression. *Geology* **12**, 550–554.

Coney, P. J. & Reynolds, S. J. (1977). Cordilleran Benioff zones. *Nature* **270**, 403–406.

DeBari, S. M. & Sleep, N. H. (1991). High-Mg, low-Al bulk composition of the Talkeetna island arc, Alaska: Implications for primary magmas and the nature of arc crust. *Geological Society of America Bulletin* **103**, 37–47.

DeCelles, P. G. (2004). Late Jurassic to Eocene evolution of the Cordilleran thrust belt and foreland basin system, western U.S.A. *American Journal of Science* **304**, 105–168.

DeCelles, P. G., Ducea, M. N., Kapp, P. & Zandt, G. (2009). Cyclicity in Cordilleran orogenic systems. *Nature Geoscience* **2**, 251–257.

Dick, H. J. B. & Bullen, T. (1984). Chromian spinel as a petrogenetic indicator in abyssal and alpine-type peridotites and spatially associated lavas. *Contributions to Mineralogy and Petrology* **86**, 54–76.

Dickinson, W. R. (1981). Plate tectonics and the continental margin of California. In: Ernst, W. G. (ed.) *The Geotectonic Development of California*. Englewood Cliffs, NJ: Prentice Hall, pp. 1–28.

Dickinson, W. R. (2004). Evolution of the North American Cordillera. *Annual Review of Earth and Planetary Sciences* **32**, 13–45.

Dickinson, W. R. & Snyder, W. S. (1978). Plate tectonics of the Laramide orogeny. In: Matthews, V. (ed.) *Laramide Folding Associated with Basement Block Faulting in the Western United States. Geological Society of America, Memoirs* **151**, 355–366.

Dodge, F. C. W., Lockwood, J. P. & Calk, L. C. (1988). Fragments of the mantle and crust from beneath the Sierra Nevada batholith: Xenoliths in a volcanic pipe near Big Creek, California. *Geological Society of America Bulletin* **100**, 938–947.

Ducea, M. N. (2001). The California Arc: thick granitic batholiths, eclogitic residues, lithospheric-scale thrusting, and magmatic flare-ups. *GSA Today* **11**, 4–10.

Ducea, M. N. (2002). Constraints on the bulk composition and root foundering rates of continental arcs: A California arc perspective. *Journal of Geophysical Research* **107**, 1–13.

Ducea, M. & Barton, M. D. (2007). Igniting flare-up events in Cordilleran arcs. *Geology* **35**, 1047–1050.

Ducea, M. N. & Saleeby, J. B. (1996). Buoyancy sources for a large, unrooted mountain range, the Sierra Nevada, California: Evidence from xenolith thermobarometry. *Journal of Geophysical Research* **101**, 8229–8244.

Ducea, M. & Saleeby, J. (1998*a*). A case for delamination of the deep batholithic crust beneath the Sierra Nevada, California. *International Geology Review* **40**, 78–93.

Ducea, M. N. & Saleeby, J. B. (1998*b*). The age and origin of a thick mafic–ultramafic keel from beneath the Sierra Nevada batholith. *Contributions to Mineralogy and Petrology* **133**, 169–185.

Dumitru, T. A., Gans, P. B., Foster, D. A. & Miller, E. L. (1991). Refrigeration of the western Cordilleran lithosphere during Laramide shallow-angle subduction. *Geology* **19**, 1145–1148.

Eggins, S. M., Woodhead, J. D., Kinsley, L. P. J., Mortimer, G. E., Sylvester, P., McCulloch, M. T., Hergt, J. M. & Handler, M. R. (1997). A simple method for the precise determination of ≥40 trace elements in geological samples by ICPMS using enriched isotope internal standardisation. *Chemical Geology* **134**, 311–326.

Ellis, D. J. & Green, D. H. (1979). An experimental study of the effect of Ca upon garnet–clinopyroxene Fe–Mg exchange equilibria. *Contributions to Mineralogy and Petrology* **71**, 13–22.

England, P. C. & Katz, R. F. (2010). Melting above the anhydrous solidus controls the location of volcanic arcs. *Nature* **467**, 700–703.

Farmer, G. L., Glazner, A. F. & Manley, C. R. (2002). Did lithospheric delamination trigger late Cenozoic potassic volcanism in the southern Sierra Nevada, California? *Geological Society of America Bulletin* **114**, 754–768.

Gao, S., Liu, X., Yuan, H., Hattendorf, B., Günther, D., Chen, L. & Hu, S. (2002). Determination of forty two major and trace elements in USGS and NIST SRM glasses by laser ablation-inductively coupled plasma-mass spectrometry. *Geostandards Newsletter* **26**, 181–196.

Green, D. H., Hibberson, W. O., Kovacs, I. & Rosenthal, A. (2010). Water and its influence on the lithosphere–asthenosphere boundary. *Nature* **467**, 448–451.

Griffin, W. L., Cousens, D. R., Ryan, C. G., Sie, S. H. & Suter, G. F. (1989). Ni in chrome pyrope garnets: a new geothermometer. *Contributions to Mineralogy and Petrology* **103**, 199–202.

Gromet, P. & Silver, L. T. (1987). REE variations across the Peninsular Ranges Batholith: implications for batholithic petrogenesis and crustal growth in magmatic arcs. *Journal of Petrology* **28**, 75–125.

Grove, T. L., Till, C. B., Lev, E., Chatterjee, N. & Medard, E. (2009). Kinematic variables and water transport control the formation and location of arc volcanoes. *Nature* **459**, 694–697.

Hanson, G. N. & Langmuir, C. H. (1978). Modelling of major elements in mantle–melt systems using trace element approaches. *Geochimica et Cosmochimica Acta* **42**, 725–741.

Harley, S. L. (1984). An experimental study of the partitioning of Fe and Mg between garnet and orthopyroxene. *Contributions to Mineralogy and Petrology* **86**, 359–373.

Harley, S. L. & Green, D. H. (1982). Garnet–orthopyroxene barometry for granulites and peridotites. *Nature* **300**, 697–701.

Hirose, K. & Kawamoto, T. (1995). Hydrous partial melting of lherzolite at 1 GPa: The effect of H_2O on the genesis of basaltic magmas. *Earth and Planetary Science Letters* **133**, 463–473.

Hofmann, A. W. (1988). Chemical differentiation of the Earth: the relationship between mantle, continental crust, and oceanic crust. *Earth and Planetary Science Letters* **90**, 297–314.

Humphreys, E. D. (1995). Post-Laramide removal of the Farallon slab, western United States. *Geology* **23**, 987–990.

Humphreys, E., Hessler, E., Dueker, K., Farmer, G., Erslev, E. & Atwater, T. (2003). How Laramide-age hydration of North American lithosphere by the Farallon Slab controlled subsequent activity in the western United States. *International Geology Review* **45**, 575–595.

Jagoutz, O., Burg, J. P., Hussain, S., Dawood, H., Pettke, T., Iizuka, T. & Maruyama, S. (2009). Construction of the granitoid crust of an island arc part I: geochronological and geochemical constraints from the plutonic Kohistan (NW Pakistan). *Contributions to Mineralogy and Petrology* **158**, 739–755.

Johnson, K. T. M., Dick, H. J. B. & Shimizu, N. (1990). Melting in the oceanic upper mantle: an ion microprobe study of diopsides in abyssal peridotites. *Journal of Geophysical Research* **95**, 2661–2678.

Jordan, T. H. (1981). Continents as a chemical boundary layer. *Philosophical Transactions of the Royal Society of London, Series A* **301**, 359–373.

Katz, R. F., Spiegelman, M. & Langmuir, C. H. (2003). A new parameterization of hydrous mantle melting. *Geochemistry, Geophysics, Geosystems* **4**, 1073.

Kay, R. W. & Kay, S. M. (1988). Crustal recycling and the Aleutian arc. *Geochimica et Cosmochimica Acta* **52**, 1351–1359.

Kelemen, P. B. (1990). Reaction between ultramafic rock and fractionating basaltic magma I. Phase relations, the origin of calc-alkaline magma series, and the formation of discordant dunite. *Journal of Petrology* **31**, 51–98.

Kelemen, P. B. (1995). Genesis of high Mg# andesites and the continental crust. *Contributions to Mineralogy and Petrology* **120**, 1–19.

Kelemen, P. B. & Hanghoj, K. (2003). One view of the geochemistry of subduction-related magmatic arcs, with an emphasis on primitive andesite and lower crust. In: Rudnick, R. L. (ed.) *Treatise on Geochemistry*. Amsterdam: Elsevier, pp. 593–659.

Kelley, K. A., Plank, T., Newman, S., Stolper, E. M., Grove, T. L., Parman, S. & Hauri, E. H. (2010). Mantle melting as a function of water content beneath the Mariana Arc. *Journal of Petrology* **51**, 1711–1738.

Kistler, R. W. (1990). Two different lithosphere types in the Sierra Nevada, California. In: Anderson, J. L. (ed.) *The Nature and Origin of Cordilleran Magmatism*. Boulder, CO: Geological Society of America, pp. 271–281.

Kistler, R. W. & Peterman, Z. E. (1973). Variations in Sr, Rb, K, Na, and initial Sr87/Sr86 in Mesozoic granitic rocks and intruded wall rocks in central California. *Geological Society of America Bulletin* **84**, 3489–3512.

Klemme, S. (2004). The influence of Cr on the garnet–spinel transition in the Earth's mantle: experiments in the system MgO–Cr_2O_3–SiO_2 and thermodynamic modelling. *Lithos* **77**, 639–646.

Krogh, E. J. (1988). The garnet–clinopyroxene Fe–Mg geothermometer—a reinterpretation of existing experimental data. *Contributions to Mineralogy and Petrology* **99**, 44–48.

Langmuir, C. H., Bezos, A., Escrig, S. & Parman, S. W. (2006). Chemical systematics and hydrous melting of mantle in back-arc basins. In: Christie, D. M. & Fisher, C. R. (eds) *Back-arc Spreading Systems: Geological, Biological, Chemical, and Physical Interactions. Geophysical Monograph, American Geophysical Union* **166**, 87–146.

Lee, C.-T., Rudnick, R. L. & Brimhall, G. H., Jr (2001). Deep lithospheric dynamics beneath the Sierra Nevada during the Mesozoic and Cenozoic as inferred from xenolith petrology. *Geochemistry, Geophysics, Geosystems* **2**, 1–27.

Lee, C.-T., Yin, Q., Rudnick, R. L., Chesley, J. T. & Jacobsen, S. B. (2000). Osmium isotopic evidence for Mesozoic removal of lithospheric mantle beneath the Sierra Nevada, California. *Science* **289**, 1912–1916.

Lee, C.-T. A. (2005). Trace element evidence for hydrous metasomatism at the base of the North American lithosphere and possible association with Laramide low-angle subduction. *Journal of Geology* **113**, 673–685.

Lee, C.-T. A., Cheng, X. & Horodyskyj, U. (2006). The development and refinement of continental arcs by primary basaltic magmatism, garnet pyroxenite accumulation, basaltic recharge and delamination: insights from the Sierra Nevada. *Contributions to Mineralogy and Petrology* **151**, 222–242.

Lee, C.-T. A., Harbert, A. & Leeman, W. P. (2007*a*). Extension of lattice strain theory to mineral/mineral rare-earth element partitioning: An approach for assessing disequilibrium and developing internally consistent partition coefficients between olivine,

orthopyroxene, clinopyroxene and basaltic melt. *Geochimica et Cosmochimica Acta* **71**, 481–496.

Lee, C.-T. A., Luffi, P. & Chin, E. J. (2011). Building and destroying continental mantle. *Annual Review of Earth and Planetary Sciences* **39**, 59–90.

Lee, C.-T. A., Morton, D. M., Kistler, R. W. & Baird, A. K. (2007*b*). Petrology and tectonics of Phanerozoic continent formation: From island arcs to accretion and continental arc magmatism. *Earth and Planetary Science Letters* **263**, 370–387.

Lipman, P. W. (1992). Magmatism in the Cordilleran United States; Progress and problems. In: Burchfiel, B. C., Lipman, P. W. & Zoback, M. L. (eds) *The Cordilleran Orogen Conterminous US. The Geology of North America* **G-3**, 481–514.

MacGregor, I. D. (1964). The reaction 4 enstatite + spinel = forsterite + pyrope. *Carnegie Institution of Washington Yearbook* **63**, p. 157.

Matsukage, K. N. & Kubo, K. (2003). Chromian spinel during melting experiments of dry peridotite KLB-1) at 1·0–2·5 GPa. *American Mineralogist* **88**, 1271–1278.

McDonough, W. F. (1990). Constraints on the composition of the continental lithospheric mantle. *Earth and Planetary Science Letters* **101**, 1–18.

McDonough, W. F. & Sun, S. s. (1995). The composition of the Earth. *Chemical Geology* **120**, 223–253.

Mercier, J.-C. C. & Nicolas, A. (1975). Textures and fabrics of upper-mantle peridotites as illustrated by xenoliths from basalts. *Journal of Petrology* **16**, 454–487.

Mukhopadhyay, B. (1989). *Petrology and geochemistry of mafic and ultramafic xenoliths from the Sierra Nevada batholith, Part I, Ph. D. dissertation*. Univ. of Texas at Dallas, p. 215.

Mukhopadhyay, B. & Manton, W. I. (1994). Upper-mantle fragments from beneath the Sierra Nevada Batholith: partial fusion, fractional crystallization, and metasomatism in a subduction related ancient lithosphere. *Journal of Petrology* **35**, 1417–1450.

Obata, M. & Morten, L. (1987). Transformation of spinel lherzolite to garnet lherzolite in ultramafic lenses of the Austridic Crystalline Complex, northern Italy. *Journal of Petrology* **28**, 599–623.

O'Neill, H. S. C. (1981). The transition between spinel lherzolite and garnet lherzolite, and its use as a geobarometer. *Contributions to Mineralogy and Petrology* **77**, 185–194.

O'Neill, H. S. C. & Wood, B. J. (1979). An experimental study of Fe-Mg partitioning between garnet and olivine and its calibration as a geothermometer. *Contributions to Mineralogy and Petrology* **70**(1), 59–70.

Putirka, K. D. (2008). Thermometers and barometers for volcanic systems. In: Putirka, K. D. & Tepley, F. J., III (eds) *Minerals, Inclusions and Volcanic Processes. Mineralogical Society of America and Geochemical Society, Reviews in Mineralogy and Geochemistry* **69**, 61–120.

Rudnick, R. L. (1995). Making continental crust. *Nature* **378**, 571–578.

Rudnick, R. L. & Gao, S. (2003). Composition of the continental crust. In: Rudnick, R. L. (ed.) *Treatise on Geochemistry Volume 3*. Elsevier, pp. 1–64.

Saleeby, J. (2003). Segmentation of the Laramide Slab—evidence from the southern Sierra Nevada region. *Geological Society of America Bulletin* **115**, 655–668.

Saleeby, J. B., Sams, D. B. & Kistler, R. W. (1987). U/Pb zircon, strontium, and oxygen isotopic and geochronological study of the southernmost Sierra Nevada Batholith, California. *Journal of Geophysical Research* **92**, 10443–10466.

Saltzer, R. L., Chatterjee, N. & Grove, T. L. (2001). The spatial distribution of garnets and pyroxenes in mantle peridotites: pressure–temperature history of peridotites from the Kaapvaal Craton. *Journal of Petrology* **42**, 2215–2229.

Sautter, V. & Fabriès, J. (1990). Cooling kinetics of garnet websterites from the Freychinède orogenic lherzolite massif, French Pyrenees. *Contributions to Mineralogy and Petrology* **105**, 533–549.

Sisson, T. W., Grove, T. L. & Coleman, D. S. (1996). Hornblende gabbro sill complex at Onion Valley, California, and a mixing origin for the Sierra Nevada batholith. *Contributions to Mineralogy and Petrology* **126**, 81–108.

Syracuse, E. M. & Abers, G. A. (2006). Global compilation of variations in slab depth beneath arc volcanoes and implications. *Geochemistry, Geophysics, Geosystems* **7**, 1–18.

Tatsumi, Y. (2005). The subduction factory: how it operates in the evolving Earth. *GSA Today* **15**, 4–10.

Van Kooten, G. K. (1980). Mineralogy, petrology, and geochemistry of an ultrapotassic basaltic suite, central Sierra Nevada, California, USA. *Journal of Petrology* **21**, 651–684.

Walter, M. J. (1998). Melting of garnet peridotite and the origin of komatiite and depleted lithosphere. *Journal of Petrology* **39**, 29–60.

Webb, S. A. C. & Wood, B. J. (1986). Spinel–pyroxene–garnet relationships and their dependence on Cr/Al ratio. *Contributions to Mineralogy and Petrology* **92**, 471–480.

Wernicke, B. (1981). Low-angle normal faults in the Basin and Range Province: nappe tectonics in an extending orogen. *Nature* **291**, 645–648.

Witt-Eickschen, G. & O'Neill, H. S. C. (2005). The effect of temperature on the equilibrium distribution of trace elements between clinopyroxene, orthopyroxene, olivine and spinel in upper mantle peridotite. *Chemical Geology* **221**, 65–101.

Witt-Eickschen, G. & Seck, H. A. (1991). Solubility of Ca and Al in orthopyroxene from spinel peridotite: an improved version of an empirical geothermometer. *Contributions to Mineralogy and Petrology* **106**, 431–439.

Zandt, G., Gilbert, H., Owens, T. J., Ducea, M., Saleeby, J. & Jones, C. H. (2004). Active foundering of a continental arc root beneath the southern Sierra Nevada in California. *Nature* **431**, 41–46.